Real space imaging of hydrogen at a metal - metal hydride interface

de Graaf, Sytze ; Momand, Jamo; Mitterbauer, Christoph; Lazar, Sorin; Kooi, Bart J.

Published in:
ArXiv

Real space imaging of hydrogen at a metal - metal hydride interface

Sytze de Graaf[1],*, Jamo Momand[1], Christoph Mitterbauer[2], Sorin Lazar[2], Bart J. Kooi[1],*

[1]Zernike Institute for Advanced Materials, University of Groningen, Nijenborgh 4, 9747 AG

Groningen, The Netherlands

[2]Thermo Fisher Scientific, Achtseweg Noord 5, 5651 GG Eindhoven, The Netherlands

* sytze.de.graaf@rug.nl, b.j.kooi@rug.nl

Abstract: Hydrogen as a prospective fuel can be stored safely with high volumetric density in metals. It can, however, also be detrimental to metals causing embrittlement. For a better understanding of these metal–metal hydride systems, and in particular their interfaces, real-space imaging of hydrogen with atomic resolution is required. However, hydrogen has not been imaged before at an interface. Moreover, to date, a robust technique that is capable to do such light-element imaging has not been demonstrated. Here, we show that integrated Differential Phase Contrast (iDPC), a recently developed imaging technique performed in an aberration corrected scanning transmission electron microscope, has this capability. Atomically sharp interfaces between hexagonal close-packed titanium and face-centered tetragonal titanium monohydride have been imaged, unambiguously resolving the hydrogen columns. Exploiting the fact that this monohydride has two types of columns with identical surrounding of the host Ti atom we have, 30 years after they were first proposed, finally resolved which one of the proposed structural models holds for the interface. Using both experimental and simulated images, we compare the iDPC technique with the currently more common annular bright field (ABF) technique, showing that iDPC is superior regarding complicating wave interference effects that may lead to erroneous detection of light element columns.

Hydrogen is the most abundant, but also the most light-weight element in the universe. Therefore its direct imaging in crystals using transmission electron microscopy (TEM) based techniques has remained elusive, despite the important role hydrogen plays in various fields such as hydrogen storage[1,2] and hydrogen embrittlement[3–5]. Not only its low weight, but particularly also the weight difference between hydrogen and the host atoms in the crystal makes direct imaging of hydrogen highly challenging. Imaging based on TEM and scanning TEM (STEM) has, after the introduction of powerful field-emission electron sources and aberration correctors, nowadays reached resolutions well below 100 pm[6,7] allowing details of most crystals to be resolved. In an aberration corrected STEM, the electrons are accelerated and focused into a sub-Å sized probe that scans across the surface of a thin specimen (Fig. 1a). The incident electrons interact with the specimen's local electrostatic fields as they propagate through the crystal and produce a scattered exit-beam of electrons that form a diffraction pattern in the detector plane.
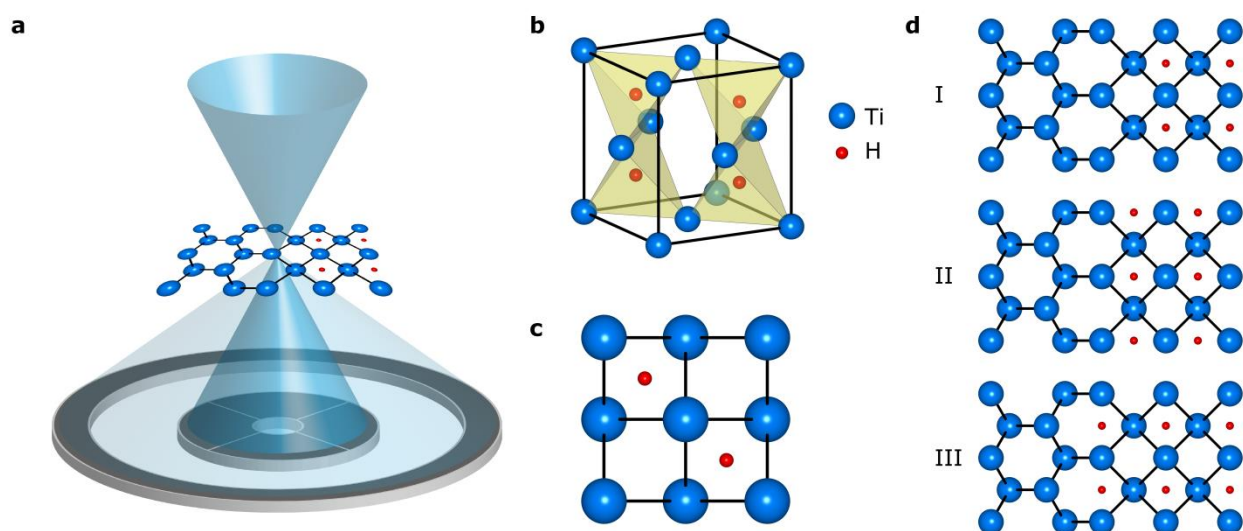
Fig. 1: Schematic of a STEM system and the γ-TiH crystal and its three possible interfaces with α-Ti.

*a, iDPC images are captured with the quadrant detector (inner) and can be used simultaneously with the HAADF detector (outer). **b**, Crystal structure model of the FCT γ-TiH unit cell containing four hydrogen atoms that occupy tetrahedral sites. **c**, Two columns in between the titanium columns are occupied with hydrogen atoms and two columns are empty. **d**, Three potential models can describe the interface between γ-TiH and α-Ti.*

The popular high-angle annular dark field (HAADF) STEM technique collects the incoherently scattered electrons at relatively high collection angles using an annular detector. This technique is not affected by the wave character of the electrons that gives interferences complicating the interpretation of images. Consequently, HAADF-STEM images are readily interpretable, as atomic columns in a crystal are always imaged as bright dots in a dark surrounding with a dot brightness scaling with the average atomic number Z in the atomic column (typically $Z^{1.6-2.0}$)[8,9]. Using this technique even single carbon atoms can be detected in graphene[10–12] and boron and nitrogen can be distinguished in 2D-BN[13]. However, materials often consist of elements with a large difference in atomic number, such as heavy metal atoms next to light atoms like oxygen, nitrogen, carbon or hydrogen, where the scattering strength of the light elements compared to the heavy element is too low to be detected. Therefore, it is not possible to image light and heavy elements simultaneously with HAADF-STEM.

In annular bright field (ABF) STEM, the collection angles are reduced drastically in order to get sufficient signal from light elements. Hydrogen has been directly imaged with ABF-STEM in bulk crystals such as YH_2[14], VH_2[15] and NbH_2[16]. However, the specimens must be very thin, i.e. preferably less than 10 nm, otherwise the signal from the hydrogen atoms cannot be detected. Unfortunately, not all materials can be thinned down to this level, due to limitations such as preparation induced damage layers, surface oxides or sample stability. In addition, the ABF-STEM technique automatically re-introduces the wave interference effects in the imaging, making unambiguous detection of the light element difficult. Consequently, ABF-STEM cannot robustly image hydrogen atoms in realistic systems and has, therefore, been limited to model materials. For this reason, hydrogen has not been imaged before at an interface, with vastly different concentrations of hydrogen on both sides of the interface, despite this being most interesting from a materials science perspective.

Here we use the recently developed integrated Differential Phase Contrast (iDPC) technique, where coherently scattered electrons that fall inside the bright-field disk are collected with an annular detector that is segmented into four quadrants (Fig. 1a)[17]. Using DPC imaging[18–23] various complementary local electrostatic properties of the specimen can be retrieved using integration/differentiation in the Fourier domain (see also supplementary information)[17]. Imaging the electrostatic potential with iDPC is particularly useful to generate sensitivity towards light

elements[24,25], because on the one hand the potential is linear with the average atomic number Z in the atomic column, and on the other hand it is proportional to the phase shift of the transmitted electron wave. This phase contrast imaging capability is desirable in electron microscopy, since thin specimens predominantly affect the phase of the electron wave and not its amplitude. Major advantages of iDPC over ABF are (1) its phase contrast imaging ability; (2) a simpler contrast transfer function, i.e. less problems with the wave interference character and contrast reversals in the images; and (3) a better signal-to-noise ratio, which in the end also provides the option to use lower doses (on vulnerable samples). Here we image hydrogen atoms for the first time at a metal-metal hydride interface using iDPC-STEM.

In order to produce stable metal - metal hydride interfaces we have chosen the Ti-TiH system, that is remarkably similar to the Zr-ZrH system, which plays an important role as nuclear fuel cladding material in nuclear reactors[8,9]. In contrast to earlier studies that image hydrogen in a di-hydride like YH_2, here we study the monohydride γ-TiH. This hydride readily forms at low temperature and low hydrogen concentrations due to the high hydrogen mobility and low (room temperature) hydrogen solubility limit in hexagonal close-packed α-Ti[9,10]. The structure of this phase has been studied by diffraction techniques already more than three decades ago[27–29]. The γ-TiH crystal has a face centred tetragonal (FCT) lattice that contains four titanium and four hydrogen atoms per unit cell (Fig. 1b). Half of the tetrahedral interstitial sites are occupied by hydrogen atoms that organize in two columns that are parallel to the c-axis and are located on the face diagonal when viewed along the c-axis (Fig. 1c). Ab-initio calculations performed on the isomorphic γ-ZrH indicate that, despite a lower entropy contribution, this ordering of hydrogen in columns is more stable than the diamond-like occupation, where the hydrogen atoms occupy alternating tetrahedral sites[30]. A similar result, although described less explicitly, was obtained for γ-TiH[31].

Imaging the monohydride offers major benefits over a di-hydride, because in single images we can image columns with identical surrounding of the host Ti atom columns where one type of column contains the hydrogen atoms and the other type in principle is empty. Since the wave character of the electrons plays a role during imaging it cannot be ruled out that a certain atomic-like signal is obtained in a column between Ti atom columns when no hydrogen atoms are present. In the monohydride the difference between the signals coming from the hydrogen filled

columns and the empty columns can be directly compared, allowing for unambiguous interpretation that is not possible in case of the di-hydride. Imaging artefacts are often a challenge: in TEM and STEM such artefacts generally will have a symmetry related to the one of the underlying host lattices. In this respect, the monohydride offers a further advantage because the symmetry of the hydrogen sublattice is distinctly different from the one of the host titanium sublattice and therefore the weak signals we measure for the hydrogen cannot be a faint displaced/distorted replica of the host.

Even though γ-TiH has an approximately 15% larger unit cell volume compared to α-Ti matrix, an apparently strain-free coherent interface is formed between them[32]. Therefore, to accommodate the volume misfit, the lattice misfit perpendicular to the interface is about 16%[9,11]. Consequently, the growth rate parallel to the interface is orders of magnitude higher than the perpendicular one resulting in plate-shaped precipitates[29,32]. The absolute position of the hydrogen atoms with respect to the interface has to date not yet been identified because diffraction techniques do not transfer translational information and real-space atomic resolution images only provided information on the position of the titanium columns[32]. Hence, there are three possible models, schematically depicted in Fig. 1d, which cannot be distinguished using earlier techniques[32]. To find the model that agrees with the actual structure found in nature a real-space atomic resolution imaging technique that has the power to resolve the hydrogen atom columns is required.

To image the interface edge-on we align the α-Ti matrix along the [0001] direction and then the FCT γ-TiH is imaged along [001]. However, the large volume expansion by the incorporation of the γ-TiH precipitate in the Ti matrix leads to a severely strained system where the misfit is accommodated plastically via dislocation motion in the Ti matrix[29,33]. Consequently, an often encountered challenge, particularly when thinning the sample to electron transparency, is that local crystal bending across the interface impedes proper atomically resolved images over the entire region of interest. Despite not being a model system due to strain, bending and large sample thickness (see supplementary information), we were able to find well aligned areas at the interface by capturing large areas with small pixel size and quick readout times of several seconds (see supplementary information). With this approach we routinely imaged the edge-on interface with minimal residual misalignment with about 60 pm resolution (Fig. 2).
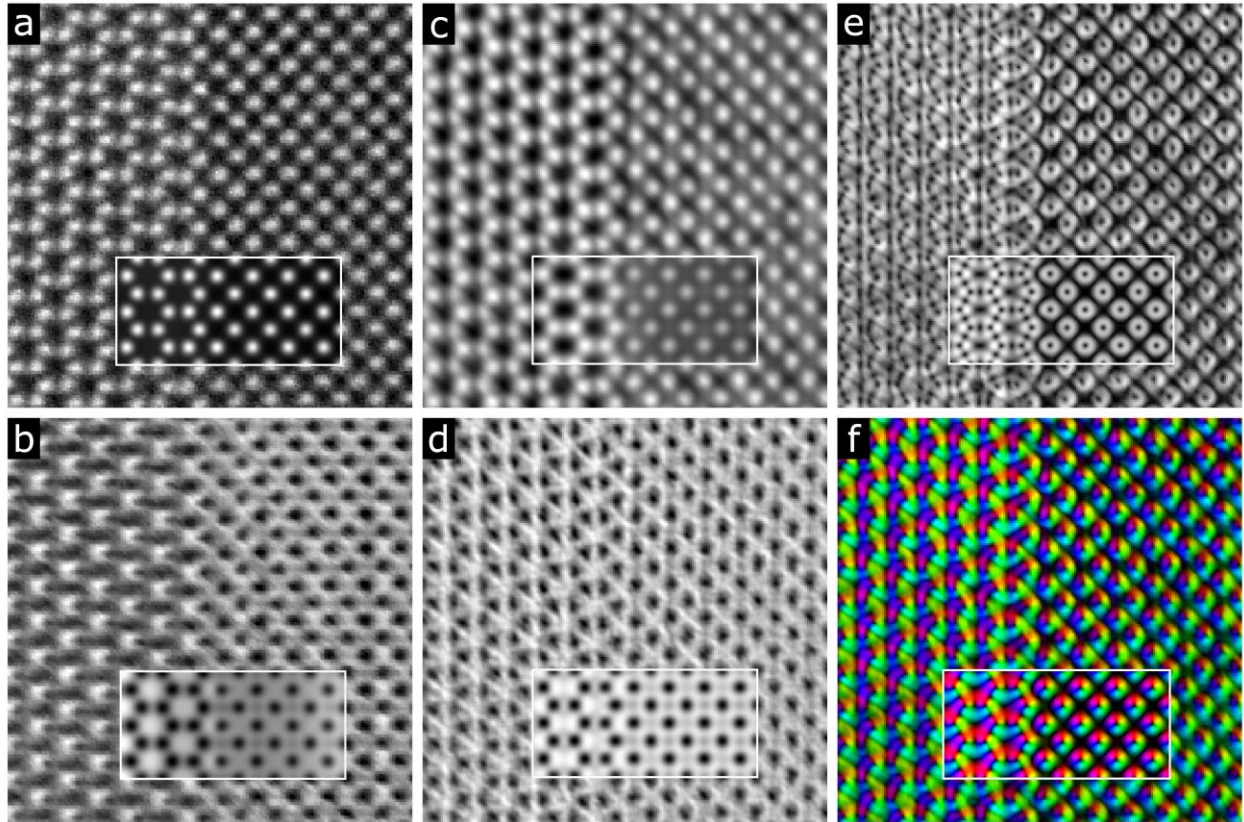
Fig. 2: Comparison of STEM images of the interface between γ-TiH and α-Ti using different techniques.

a, HAADF. b, ABF. c, iDPC. d, dDPC. e, DPC magnitude. f, DPC vector field using colour wheel representation. Simulated images of a 30 nm thick specimen are inset in the image. Field of view is 3.5x3.5 nm.

The image recorded with the HAADF detector can be interpreted directly by virtue of Z-contrast: it shows two clearly distinguishable lattices separated by an atomically sharp interface that matches convincingly with the simulated image (Fig. 2a). Viewed along these crystal axes, the α-Ti(01-10) planes are parallel to the γ-TiH(1-10) planes at the interface, which is in agreement with the TEM studies that were performed over three decades ago[29,32]. Although the Z-contrast image exclusively visualizes the titanium atoms, it fails to transfer signal from the hydrogen atoms which are expected in equivalent stoichiometry in the γ-TiH.

Next we used ABF to image the α-Ti/γ-TiH interface (Fig. 2b), although the specimen thickness of about 30 nm is thicker than required to properly image hydrogen atoms with ABF. The

titanium atoms are well-resolved as dips in intensity in the γ-TiH but poorly in the α-Ti. The high sensitivity of ABF imaging towards crystal orientation (see Fig. S11) combined with the inherent local bending of the specimen leads to the lower quality of the ABF image compared to the HAADF image[34]. Nonetheless, in the γ-TiH part of the image a weak contrast is visible between alternating atomic planes parallel and perpendicular to the interface that indicates the presence of signal from the hydrogen columns. Close inspection suggests that either model I or III best describes the interface (Fig. 1d). However, being limited by the signal-to-noise ratio and quality of the image we cannot reliably determine the exact position of hydrogen columns.

As a final step, four complementary images depicted in Fig. 2c-f were recorded for the same interface region with the segmented detector. These images represent atomic scale electrostatic properties of the specimen. The projected electrostatic potential is captured in the iDPC image, where the Ti atoms in the γ-TiH as well as the α-Ti matrix are resolved accurately (Fig. 2c). Besides the bright Ti atoms, there is a clear signal within the γ-TiH crystal that forms a checkerboard-like pattern with the symmetry that is expected for the hydrogen sublattice. With the convincing match between the experimental and simulated image, and the extensive image simulations that we have performed (see supplementary information), we show that the hydrogen columns are indeed imaged with iDPC and that the interface is best described by model I (Fig. 1d).

Despite that the γ-TiH is a metastable phase and hydrogen is very mobile in titanium, even at room temperature, we did not observe any structural changes during the imaging. This is rather remarkable considering the energetic electrons impinging on the specimen and the step function in hydrogen concentration of about 50 atomic percent across the interface. The absence of structural changes is most likely caused by the stabilizing effect the α-Ti has on the γ-TiH phase via the interface. Ab-initio simulations[9] have demonstrated that on the one hand the stability of α-Ti rapidly decreases when hydrogen is inserted in interstitial sites, which is expected, considering its low room-temperature hydrogen solubility limit. On the other hand, coherency strains at the interface have been shown to be key for stabilizing the γ-TiH phase. Moreover, the huge (15%) volume expansion, requiring full accommodation perpendicular to the interface, reveals the barrier hydrogen atoms experience when they jump from the γ-TiH across the interface into the α-Ti.

The specimen's charge density is imaged with differentiated DPC (dDPC) (Fig. 2d) and has a negative contrast transfer function similar to ABF (Fig. 2b). In the dDPC image the Ti atoms are properly resolved throughout the image, in contrast to the ABF image where they were only well resolved in the γ-TiH. As in the ABF image, the signal from the hydrogen columns is faint and limited by the signal-to-noise ratio, preventing accurate hydrogen column detection in the image. The projected electric field is revealed in the DPC images in Figs. 2e and f. Fig. 2e shows the scalar field strength, and 2f the vector field, where the field direction is indicated by the colour and the strength by the intensity. Fig. 2e displays a rather complex field in the Ti matrix, and a more easily interpretable field in the γ-TiH which agrees well with the simulation. The field strength at the Ti atom columns in the γ-TiH are not radially symmetric, but ellipse shaped with the long-axis oriented in two orthogonal directions. This is a direct effect of the subtle electric field from the checkerboard-like ordered hydrogen columns and allows us to confirm model I as the best description of the interface.

We compare the Fourier Transforms (FT) of the images to investigate why the iDPC image has the clearest signal from the hydrogen atoms compared to the other imaging techniques. In Fig. 3a-d we show the fast FT (FFT) of the full source images from Fig. 2a-d, respectively, where the symmetry of the α-Ti and γ-TiH lattices are also indicated. The checkerboard-like ordering of the hydrogen columns in γ-TiH is present as super-reflections in the FFTs of the images. The relative intensity of the γ-TiH{110} super-reflections with respect to an allowed reflection (here we use the γ-TiH{200} peaks as reference) indicates how well the long-range ordering of hydrogen columns is defined in the image. The four intensity profiles that connect the γ-TiH{200} peaks are averaged and shown in Fig. 3e. From these peaks the relative {110}/{200} intensity is calculated and inset in the FFTs. In the case of the HAADF image there is no {110} peak presents, but only a minor amount of streaking intensity that originates from the nearby α-Ti{10-10} peaks. In the dDPC image the relative intensity is close to half the value of the ABF and iDPC images. The ABF and iDPC images contain the highest relative strength of the super-reflections and are remarkably similar, indicating that the long-range {110} ordering of the hydrogen columns is equally present in both images. Despite this similarity of the ABF and iDPC images in reciprocal space, the iDPC image has a significantly better short-range transfer of intensity of the hydrogen columns in real space (compare Figs. 2b and c). The relevant physical

reasons are the reasonably thick specimen and inherent bending that drastically reduce the signal from the hydrogen columns for ABF and substantially less for iDPC (see Fig. S7 and S11). In addition, the signal-to-noise ratio of iDPC compared to ABF is improved because on the one hand the segmented detector collects more electrons, while on the other hand the random noise is suppressed by physical regularization[17,35].
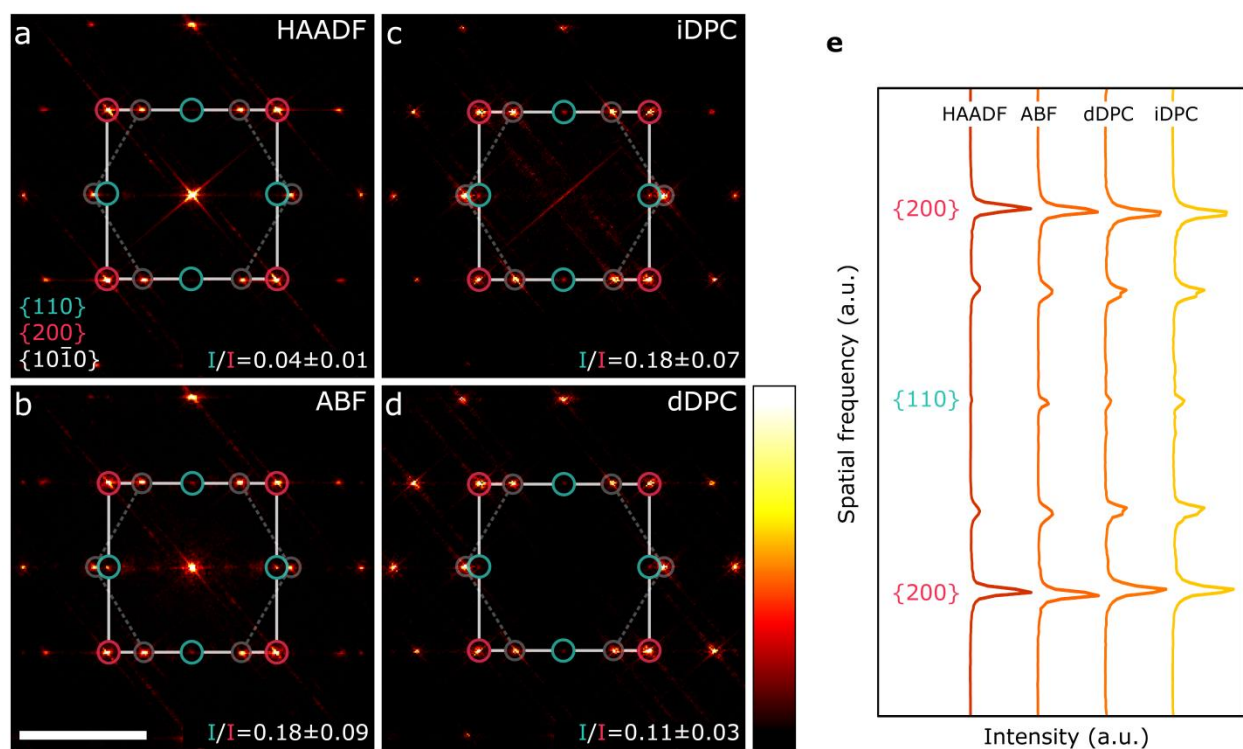

Fig. 3: Comparison of the hydrogen signal in the FFTs of the real space images of the interface between γ-TiH and α-Ti.

a, HAADF. b, ABF. c, iDPC. d, dDPC. Dashed and solid lines connect the encircled low-index reflections from the HCP α-Ti and FCT γ-TiH lattices, respectively. Scale bar size is 5.0 nm⁻¹. e, Averaged intensity profiles of the four lines connecting the γ-TiH{200} reflections encircled in red, from which the relative intensity γ-TiH{110}/γ-TiH{200} is calculated and inset in the bottom-right of a-d.

A quantitative comparison between experimental and simulated iDPC images is shown in Fig. 4. The experimental intensity profiles of the atomic planes perpendicular to the interface in the γ-TiH of the iDPC image Fig. 2c are averaged separately for the alternating planes containing

hydrogen columns (Ti-H-Ti) and for the intermediate planes containing empty columns (Ti-empty-Ti). The resulting two experimental profiles together with the simulated profiles are plotted in Fig. 4a. We extracted the profiles from a simulated 32.2 nm thick specimen, despite that the experimental and simulated intensity profiles match approximately equally well for 30 to 50 nm thick specimen (see Fig. S12). In this range the relative intensity of the titanium, hydrogen and empty column remain rather constant (see Fig. 4b and more quantitatively Fig. S10). This is an advantage of iDPC as its hydrogen imaging capability is not sensitive to specimen thickness.
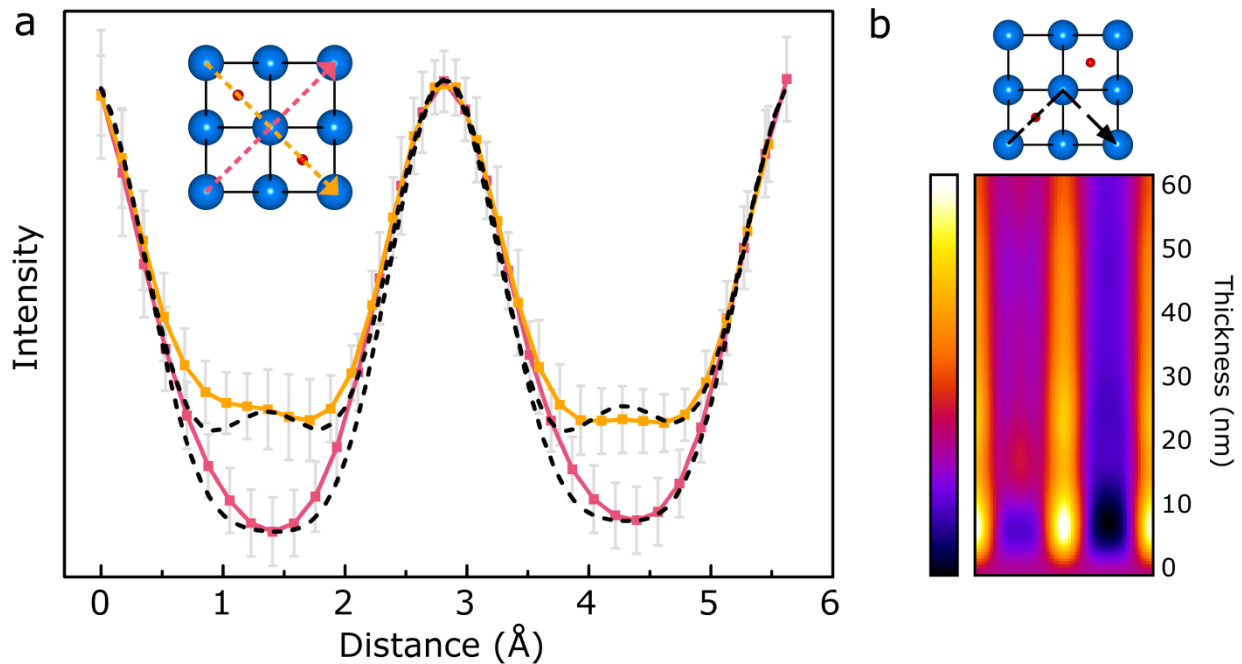

Fig. 4: Comparison of experimental and simulated iDPC intensity profiles.

a, Averaged experimental iDPC intensity profiles obtained from Fig. 2c shown in pink and yellow solid lines. Error bars indicate the standard deviations. Pink line represent the Ti-empty-Ti-empty-Ti columns, and the yellow line represent the Ti-H-Ti-H-Ti columns. Dashed lines are the simulated results of a 32.2 nm thick γ-TiH crystal. b, Simulated intensity profile as a function of specimen thickness of the path drawn in the γ-TiH model, containing Ti-H-Ti-empty-Ti columns.

Thus, our extensive image simulations of the γ-TiH unit cell (see supplementary information) and experimental images allow us to conclude that iDPC has several advantageous over ABF

imaging. iDPC images the hydrogen columns with higher contrast and better localization. The atom column intensity oscillates substantially less as a function of specimen thickness. Contrast also does not reverse as long as the probe is focused into the specimen, unlike ABF imaging where the empty column and hydrogen filled column reverse contrast for specimen thinner than about 10 nm. These simulation results clearly demonstrate that on fairly all aspects iDPC images allow more straightforward interpretation and better imaging of the light element column next to an empty column. In ABF the signal coming from the hydrogen column and the empty column are very similar and can reverse which shows that ABF is prone to erroneous detection of light elements.

From Fig. 4 it can be derived that the peak at the position of hydrogen columns is not so well defined for the experimental iDPC image that was captured at the α-Ti/γ-TiH interface, compared to the simulation. The predominant reason for this is that strain and crystal bending at the interface limit the quality of the experimental images. Due to the random imperfections in the crystal (Fig. S4) it is essential to capture high resolution images of large areas as fast as possible to locally obtain the highest possible quality atomically resolved images while minimizing drift. In this context, the iDPC-STEM technique has a clear advantage over the recent demonstration of ptychographic reconstructions[36–40] where a complete diffraction pattern is captured with a pixelated detector at every scan position. From this large 4D dataset the local phase change of the electron wave can be retrieved using an iterative phase retrieval algorithm. However, the image resolution is currently limited by the two orders of magnitude longer pixel dwell time[36]. Hence, for imperfect systems like presented here iDPC has an advantage.

Higher quality images of the γ-TiH can be captured further away from the interface where the crystal strain has relieved and local bending is much less a problem (Fig. 5). A result is that the hydrogen columns appear more localized compared to the images that are recorded at the interface. Now the checkerboard-like filling of the hydrogen columns in the γ-TiH lattice is clearly visible in Fig. 5b which is lacking in the HAADF-STEM image in Fig. 5a. Here we constructed the ABF image by summing the four images from the quadrant detectors. The outer collection angle is larger than usual for ABF imaging, but similar collection angles have been used to image hydrogen in VH_2[15]; our simulations show that then higher hydrogen column intensity can be achieved at the costs of localization (Fig. S7). Indeed, now the hydrogen columns

are also readily observable next to the titanium ones in the ABF image. Nevertheless, the iDPC image has still significantly higher signal-to-noise ratio compared to the ABF image. This result emphasizes the intrinsic random noise suppressing ability of the iDPC imaging technique, considering that the ABF and iDPC images are constructed from the same signal.
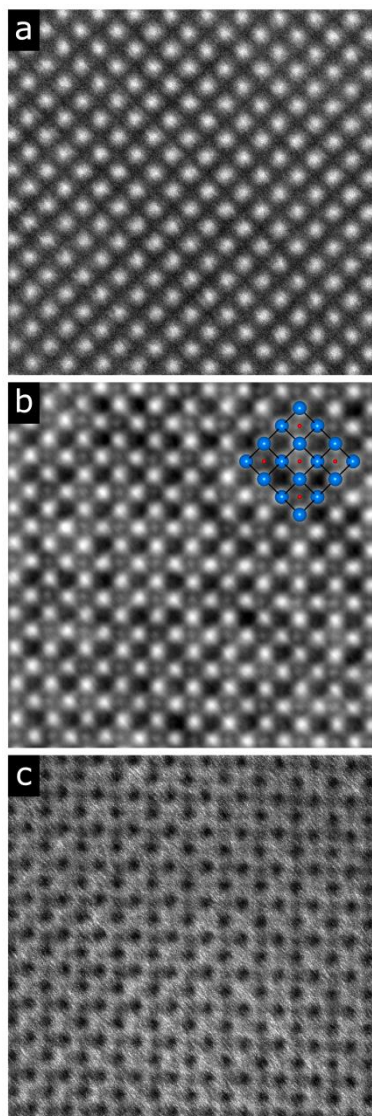

Fig. 5: Comparison of high-quality STEM images of γ-TiH far away from the interface.

a, HAADF. b, iDPC. c, ABF. Field of view is 3.13x3.13 nm.

In summary, using the recently developed iDPC-STEM technique, we have, for the first time succeeded in imaging hydrogen atom columns inside γ-TiH at the interface with α-Ti. Unambiguous detection of the hydrogen columns was greatly facilitated by the fact that in γ-TiH only half of the interstitial columns between the Ti columns are filled with hydrogen atoms and so we could directly compare filled and empty columns both in experimental and simulated images. Thus, thirty years after three models were proposed for the positions of the hydrogen columns with respect to the interface we have been able to confirm model I as the correct model. Our investigation shows that the iDPC technique reduces wave character behaviour, enhances signal-to-noise ratio and has phase contrast imaging capability even for thick specimens, indicating that iDPC has several advantages over ABF STEM. Significantly, our non-ideal material system with severe and limiting imperfections demonstrates the ability and the prospects of iDPC-STEM as a potential robust tool in material research for analysing alloys and compounds containing light elements next to heavy ones, like oxides, nitrides, carbides, borides and hydrides.

Methods

Specimen preparation. A single crystal titanium sample was mechanically polished followed by twin-jet electrochemical polishing at room temperature with a TenuPol-3 from Struers, to load the sample with hydrogen such that the γ-TiH precipitates were formed. A TEM lamella was extracted from the sample using a Helios G4 CX dual beam system with a Ga focused ion beam. The lamella was thinned to electron transparency with the focused ion beam using progressively lower accelerating voltages. As a final step a Gatan PIPS II polishing system was used to polish the lamella with 0.3 kV Ar ions.

Scanning transmission electron microscopy. For the imaging we used a probe and image corrected Thermo Scientific^{TM} Themis Z S/TEM system operating at 300 kV. The specimen was plasma cleaned for three minutes prior to insertion in the S/TEM column. For the imaging a convergence semi-angle of 21 mrad was used, and the current was set to 50 pA for Fig. 2 and 14 pA for Fig. 5.

Multislice simulations. The crystallographic models of the γ-TiH unit cell and the γ-TiH/α-Ti interface were constructed with VESTA. The γ-TiH unit cell was adjusted ($< 2\%$ change in lattice parameters) to obtain a coherent interface with α-Ti. These models were loaded in the Dr.Probe software for STEM image simulations. Microscope parameters were set equal to experimentally calibrated values, and aberrations were neglected. Images were simulated as a function of defocus and sample thickness. The detectors collection angles were also set to the experimentally calibrated values. The resulting images were convolved with a two-dimensional Gaussian function of 70 pm FWHM to account for finite probe size.

References

1. Schlapbach, L. & Züttel, A. Hydrogen-storage materials for mobile applications. *Nature* **414**, 353–358 (2001).

2. Sakintuna, B., Lamari-Darkrim, F. & Hirscher, M. Metal hydride materials for solid hydrogen storage: A review. *Int. J. Hydrog. Energy* **32**, 1121–1140 (2007).

3. Song, J. & Curtin, W. A. Atomic mechanism and prediction of hydrogen embrittlement in iron. *Nat. Mater.* **12**, 145–151 (2013).

4. Barnoush, A. & Vehoff, H. Recent developments in the study of hydrogen embrittlement: Hydrogen effect on dislocation nucleation. *Acta Mater.* **58**, 5274–5285 (2010).

5. Daw, M. S. & Baskes, M. I. Semiempirical, Quantum Mechanical Calculation of Hydrogen Embrittlement in Metals. *Phys. Rev. Lett.* **50**, 1285–1288 (1983).

6. Erni, R., Rossell, M. D., Kisielowski, C. & Dahmen, U. Atomic-Resolution Imaging with a Sub-50-pm Electron Probe. *Phys. Rev. Lett.* **102**, 096101 (2009).

7. Sawada, H. *et al.* STEM imaging of 47-pm-separated atomic columns by a spherical aberration-corrected electron microscope with a 300-kV cold field emission gun. *J. Electron Microsc. (Tokyo)* **58**, 357–361 (2009).

8. Rafferty, B., Nellist, D. & Pennycook, J. On the origin of transverse incoherence in Z-contrast STEM. *J. Electron Microsc. (Tokyo)* **50**, 227–233 (2001).

9. Wang, Z. W. *et al.* Quantitative Z-contrast imaging in the scanning transmission electron microscope with size-selected clusters. *Phys. Rev. B* **84**, 073408 (2011).

10. Zan, R., Bangert, U., Ramasse, Q. & Novoselov, K. S. Metal−Graphene Interaction Studied via Atomic Resolution Scanning Transmission Electron Microscopy. *Nano Lett.* **11**, 1087–1092 (2011).

11. Sawada, H., Sasaki, T., Hosokawa, F. & Suenaga, K. Atomic-Resolution STEM Imaging of Graphene at Low Voltage of 30 kV with Resolution Enhancement by Using Large Convergence Angle. *Phys. Rev. Lett.* **114**, 166102 (2015).

12. Chen, B. *et al.* Dynamics of GeSbTe phase-change nanoparticles deposited on graphene. *Nanotechnology* **29**, 505706 (2018).

13. Krivanek, O. L. *et al.* Atom-by-atom structural and chemical analysis by annular dark-field electron microscopy. *Nature* **464**, 571–574 (2010).

14. Ishikawa, R. *et al.* Direct imaging of hydrogen-atom columns in a crystal by annular bright-field electron microscopy. *Nat. Mater.* **10**, 278–281 (2011).

15. Findlay, S. D. *et al.* Direct Imaging of Hydrogen within a Crystalline Environment. *Appl. Phys. Express* **3**, 116603 (2010).

16. Kim, Y.-J., Tao, R., Klie, R. F. & Seidman, D. N. Direct Atomic-Scale Imaging of Hydrogen and Oxygen Interstitials in Pure Niobium Using Atom-Probe Tomography and Aberration-Corrected Scanning Transmission Electron Microscopy. *ACS Nano* **7**, 732–739 (2013).

17. Lazić, I., Bosch, E. G. T. & Lazar, S. Phase contrast STEM for thin samples: Integrated differential phase contrast. *Ultramicroscopy* **160**, 265–280 (2016).

18. Dekkers, N.H. & de Lang, H. Differential Phase Contrast in a STEM. *Optik* **41**, 452–456 (1974).

19. Dekkers, N. H. & de Lang, H. Detection method for producing phase and amplitude images simultaneously in a scanning transmission electron microscope. *Philips Tech. Rev.* **37**, 1–9 (1977).

20. Rose, H. Nonstandard imaging methods in electron microscopy. *Ultramicroscopy* **2**, 251–267 (1977).

21. Shibata, N. *et al.* Differential phase-contrast microscopy at atomic resolution. *Nat. Phys.* **8**, 611 (2012).

22. Nellist, P. D. Electron microscopy: Atomic resolution comes into phase. *Nat. Phys.* **8**, 586 (2012).

23. Close, R., Chen, Z., Shibata, N. & Findlay, S. D. Towards quantitative, atomic-resolution reconstruction of the electrostatic potential via differential phase contrast using electrons. *Ultramicroscopy* **159**, 124–137 (2015).

24. Yücelen, E., Lazić, I. & Bosch, E. G. T. Phase contrast scanning transmission electron microscopy imaging of light and heavy atoms at the limit of contrast and resolution. *Sci. Rep.* **8**, 2676 (2018).

25. Gauquelin, N. *et al.* Determining oxygen relaxations at an interface: A comparative study between transmission electron microscopy techniques. *Ultramicroscopy* **181**, 178–190 (2017).

26. Carpenter, G. J. C. The precipitation of γ-zirconium hydride in zirconium. *Acta Metall.* **26**, 1225–1235 (1978).

27. Woo, O. T., Weatherly, G. C., Coleman, C. E. & Gilbert, R. W. The precipitation of γ-deuterides (hydrides) in titanium. *Acta Metall.* **33**, 1897–1906 (1985).

28. Woo, O. T. & Carpenter, G. J. C. γ-TiH: An isomorph of γ-ZrH. *Scr. Metall.* **19**, 931–934 (1985).

29. Numakura, H. & Koiwa, M. Hydride precipitation in titanium. *Acta Metall.* **32**, 1799–1807 (1984).

30. Domain, C., Besson, R. & Legris, A. Atomic-scale Ab-initio study of the Zr-H system: I. Bulk properties. *Acta Mater.* **50**, 3513–3526 (2002).

31. Xu, Q. & Van der Ven, A. First-principles investigation of metal-hydride phase stability: The Ti-H system. *Phys. Rev. B* **76**, 064207 (2007).

32. Bourret, A., Lasalmonie, A. & Naka, S. In-situ high resolution observation of hydride precipitation in titanium. *Scr. Metall.* **20**, 861–866 (1986).

33. Shih, D. S., Robertson, I. M. & Birnbaum, H. K. Hydrogen embrittlement of α titanium: In situ tem studies. *Acta Metall.* **36**, 111–124 (1988).

34. Findlay, S. D. *et al.* Dynamics of annular bright field imaging in scanning transmission electron microscopy. *Ultramicroscopy* **110**, 903–923 (2010).

35. Lazić, I. & Bosch, E. G. T. Chapter Three - Analytical Review of Direct Stem Imaging Techniques for Thin Samples. in *Advances in Imaging and Electron Physics* (ed. Hawkes, P. W.) **199**, 75–184 (Elsevier, 2017).

36. Jiang, Y. *et al.* Electron ptychography of 2D materials to deep sub-ångström resolution. *Nature* **559**, 343–349 (2018).

37. Yang, H. *et al.* Simultaneous atomic-resolution electron ptychography and Z-contrast imaging of light and heavy elements in complex nanostructures. *Nat. Commun.* **7**, 12532 (2016).

38. Yang, H., Ercius, P., Nellist, P. D. & Ophus, C. Enhanced phase contrast transfer using ptychography combined with a pre-specimen phase plate in a scanning transmission electron microscope. *Ultramicroscopy* **171**, 117–125 (2016).

39. Yang, H. *et al.* Electron ptychographic phase imaging of light elements in crystalline materials using Wigner distribution deconvolution. *Ultramicroscopy* **180**, 173–179 (2017).

40. Rodenburg, J. M. Ptychography and Related Diffractive Imaging Methods. in *Advances in Imaging and Electron Physics* (ed. Hawkes) **150**, 87–184 (Elsevier, 2008).

Supplementary information for:

Real space imaging of hydrogen at a metal-metal hydride interface

Sytze de Graaf[1,*], Jamo Momand[1], Christoph Mitterbauer[2], Sorin Lazar[2], Bart J. Kooi[1,*]

[1]Zernike Institute for Advanced Materials, University of Groningen, Nijenborgh 4, 9747 AG Groningen, The Netherlands

[2]Thermo Fisher Scientific, Achtseweg Noord 5, 5651 GG Eindhoven, The Netherlands

* sytze.de.graaf@rug.nl, b.j.kooi@rug.nl

1. Specimen preparation and characteristics

Disks with a diameter of 3.05 mm diameter and a thickness of about 350 μm thick were spark eroded from a titanium single crystal having a purity of 99.99% (as purchased from Goodfellow). The disks were mechanically polished on both sides to a final thickness of about 50-60 μm using sequentially 1000, 2000 and 4000 grit SiC grinding paper. The mechanically polished disks were twin-jet electrochemically polished at room temperature using a TenuPol-3 from Struers. For the electrolyte a mixture of 600 ml methanol, 360 ml 2-butoxyethanol and 64 ml of perchloric acid (72%) was used. The applied bias voltage was 10 V, with maximum flowrate (10) of the electrolyte and maximum photosensitivity (10) of the photodiode. This resulted in a constant polishing current of 100 mA for 20 seconds until the polishing device detected perforation and stopped the polishing.

During this process of electrochemical polishing plate-shaped precipitates are produced within the titanium which (in a later stage) can be identified as γ-TiH. This process of hydride formation during electrochemical polishing is well-known[1–4]. During this process the surface oxide on the titanium is continuously etched away into the liquid allowing hydrogen dissolution in the solid titanium. Since the solubility limit of hydrogen in Ti is low, the hydrogen easily precipitates in the form of thin γ-TiH platelets. We spent considerable time in characterizing and optimizing the electrochemical polishing process in order to obtain a desired structure with relatively long planar interfaces of the γ-TiH platelets in the Ti matrix without too much stresses and bending of the thin foil.

We analysed the crystal orientation of the disk using electron backscatter diffraction (EBSD) in an FEI Nova NanoSEM 650 equipped with an Ametek EDAX-TSL EBSD system. A result from this analysis is shown in **Figure S1**; it can be concluded that the sample consists mostly out of a millimetre sized grain with the c-axis tilted about 35° from the plane normal. However, there are also micrometre thick bands, extending throughout the millimetre sized crystal, that have the c-axis approximately in plane.
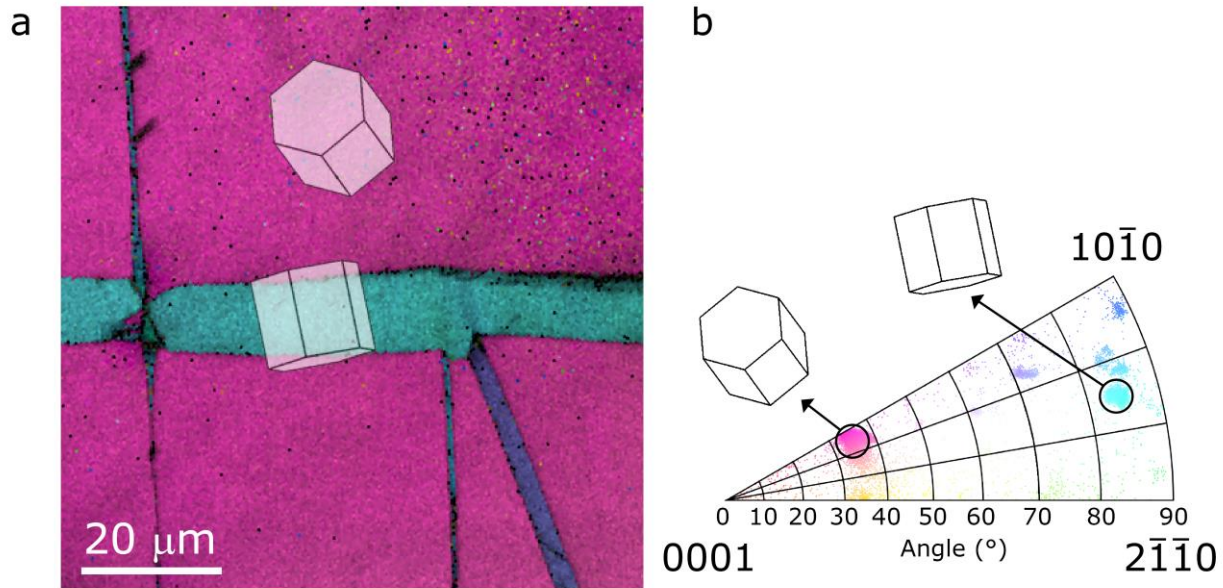

***Figure S1**: Electron back-scatter diffraction (EBSD) results of the Ti sample. **(a)** Orientation imaging microscopy image reveals two dominant grain orientations. The corresponding inverse pole figure **(b)** shows that the c-axis of the larger (purple) grain is tilted about 35° with respect to the plane normal and the thin (turquoise) band has its c-axis 85° from the plane normal, or 5° from being in plane.*

To obtain specimen with the desired c-axis normal to the sample plane we extracted lamellae from these thinner bands using a Helios G4 CX dual beam system with a Ga focused ion beam (FIB) (see **Figure S2**). A lamella was attached to a Cu TEM grid and thinned to electron transparency using progressively lower accelerating voltage from 30 kV down to 1 kV. During this stage the plate-shaped precipitates can be observed readily and they even show some further growth. The FIB thinned lamella was finally polished for 60 seconds on each side using a Gatan PIPS II Argon ion polishing system operating in stationary mode at 0.3 kV with gun angles of

±10°. Prior to S/TEM imaging, we plasma cleaned the TEM grid with the FIB lamella for three minutes with a Fischione Model 1070 plasma cleaner, using a gas mixture of 25% O_2 and 75% Ar.
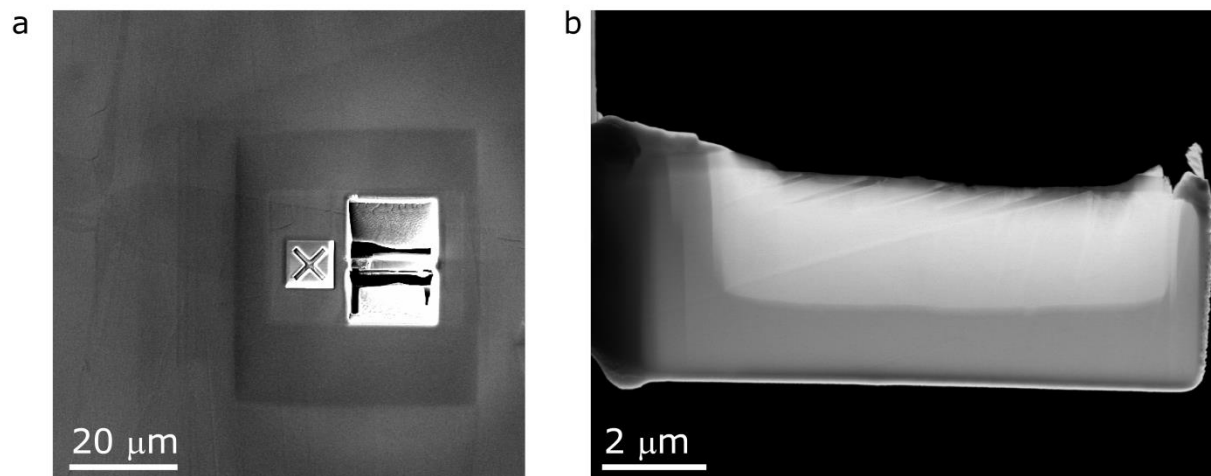

Figure S2: The extraction site and the thinned lamella are shown. (a) SEM overview image shows that we extracted a lamella from the exact same thin band as in Fig. S1a, to obtain a c-axis oriented crystal. (b) The final focused ion beam thinned lamella contains visible needle shaped precipitates oriented from bottom-left to top-right.

An overview image of the most right γ-TiH precipitate that is also visible in Figure S2b is shown in **Figure S3a**. Despite the careful thinning procedure, we observed with S/TEM that the γ-TiH precipitates are amorphous close to the edge of the lamella where the foil is the thinnest (see **Figure S3b**). As a consequence we were forced to image the interface relatively far away from the edge. For example, the images of the interface that we present in Figure 2 of the main article are captured from an area indicated by the white rectangle in Fig, S3a. This area is approximately 100 nm away from the edge, and we estimate the local thickness to be in the range of 30-40 nm based on careful comparison with image simulations.

In bright-field TEM analysis we observe bending contours that extend far into the specimen (i.e. covering all areas that are still relatively thin). The crystal bending is a feature of the specimen that is inherent to the incorporation of the γ-TiH precipitates, with about 15% larger unit cell volume compared to the host Ti. With the Kikuchi patterns that we used to align the crystal we observed that the smallest length scale of the crystal bending is of the order of several

nanometres. The crystal was also bend across the lamella with a periodicity of the order of hundreds of nanometres, however this is irrelevant considering the used field-of-view during imaging. After aligning the crystal as good as the specimen allowed at low magnification (with a field-of-view several hundreds of nanometres), we used the Kikuchi pattern to find areas close to the interface that were correctly aligned. With this approach we were able to capture the interface with atomic resolution; however a new issue that we encountered many times is that only one of the two phases, either the α -Ti or the γ-TiH, was properly resolved.
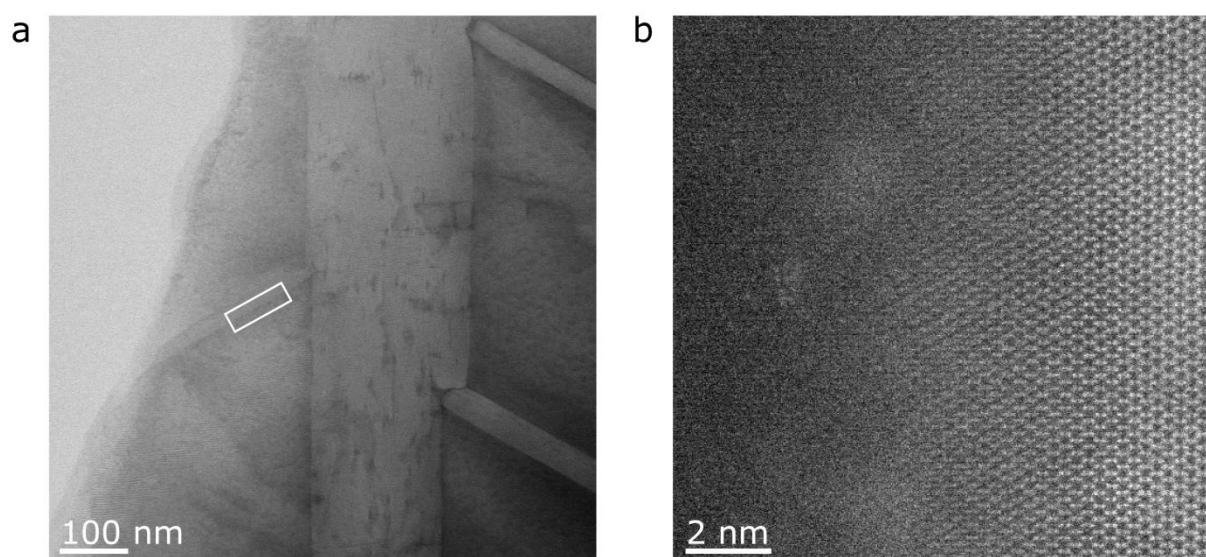

Figure S3: (a) Overview ABF-STEM image shows the γ-TiH precipitates in the α-Ti matrix. The images of the interface (Fig. 2 in the main article) were captured in the area indicated by the white rectangle. (b) The HAADF-STEM image of the interface of the central thickest precipitate that was captured close to the thin edge of the lamella. It shows that the γ-TiH precipitate (on the left) is amorphous unlike the α-Ti host (on the right) which remains crystalline.

An example that shows the crystal misalignment along the interface is depicted in Figure S4. Here the interface was imaged with atomic resolution using HAADF-STEM (**Figure S4a**) and iDPC-STEM (**Figure S4b**) simultaneously. In the HAADF-STEM image both crystals are resolved with high quality at the top of the image, but the quality starts to degrade from around the centre towards the bottom of the image. We note that the interface is not atomically sharp, however this is not necessary to demonstrate the point here. At the lower part of the image the closest Ti columns in the host matrix are not separately resolved, but form streaks perpendicular

to the interface. This is an effect of local stresses in the system (especially perpendicular to the interface where there is a 16% lattice mismatch between the precipitate and the matrix) that induce crystal bending such that the close Ti columns form streaks in projection. The misalignment of the Ti matrix is more apparent in the iDPC-STEM image, where only in the top 5 nm the α-Ti and γ-TiH are of rather good quality. In the remaining part of the image the Ti matrix forms streaks similarly to the HAADF-STEM image.

Considering all these characteristic imperfections of the specimen, we had to find areas where the local stresses were minimal such that both phases at the interface could be resolved with atomic resolution. In practice this means that we (1) aligned the crystal locally at relatively low magnification as good as possible (2) captured several images with high resolution (e.g. 1024x1024 pixels up to 4096x4096 pixels) and step sizes of 5 up to 25 pm with a pixel dwell time of 5-10 μs (3) selected well aligned parts of the image based on the combined quality of the simultaneously acquired HAADF and iDPC or ABF image.
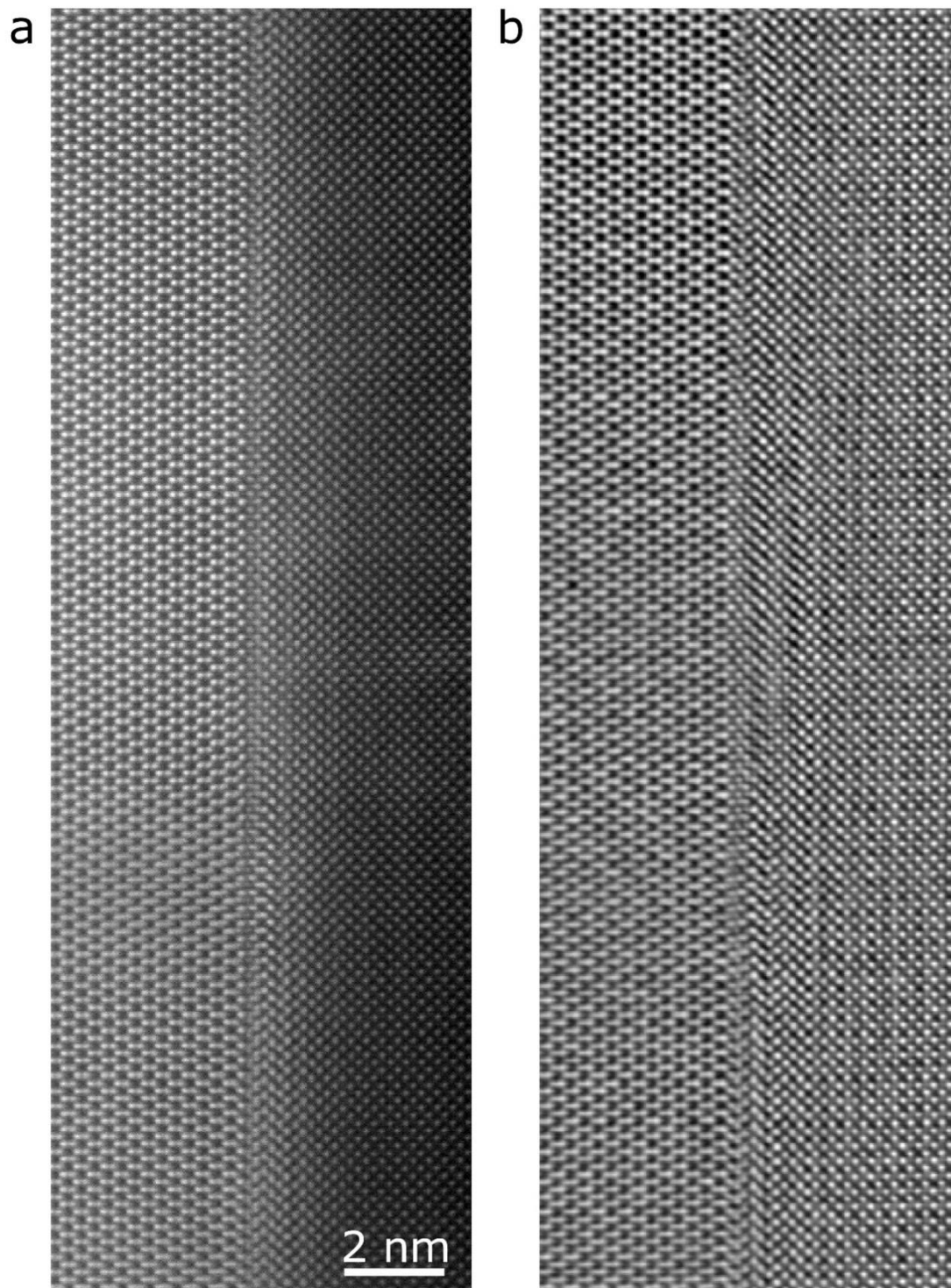
Figure S4*: Crystal bending along the interface is shown.* (***a***) *HAADF-STEM image shows that the Ti matrix gradually misaligns from top to bottom (which is about 25 nm).* (***b***) *In the iDPC-STEM image only the top 5 nm is well-aligned. Note, however, that the hydrogen columns are properly resolved in the γ-TiH precipitate along the entire interface.*

2. Electron energy loss spectroscopy

We acquired spatially resolved electron energy loss spectra (EELS) of areas containing the Ti matrix and the γ-TiH precipitates with a Thermo Scientific^{TM} Themis Z S/TEM system operating at 300 kV equiped with a Gatan Enfinium 977 system. Spectra were extracted from equally sized areas in the Ti matrix and γ-TiH precipitate (**Figure S5**). From the low electron energy loss part we obtain the locations of the plasmon peaks in Ti and in γ-TiH at 17.6 eV and 19.4 eV, respectively, which matches well with previous studies (typically 17.6 eV and 19.6 eV) [2,3] and thus can be used as a verification that γ-TiH precipitates are formed.
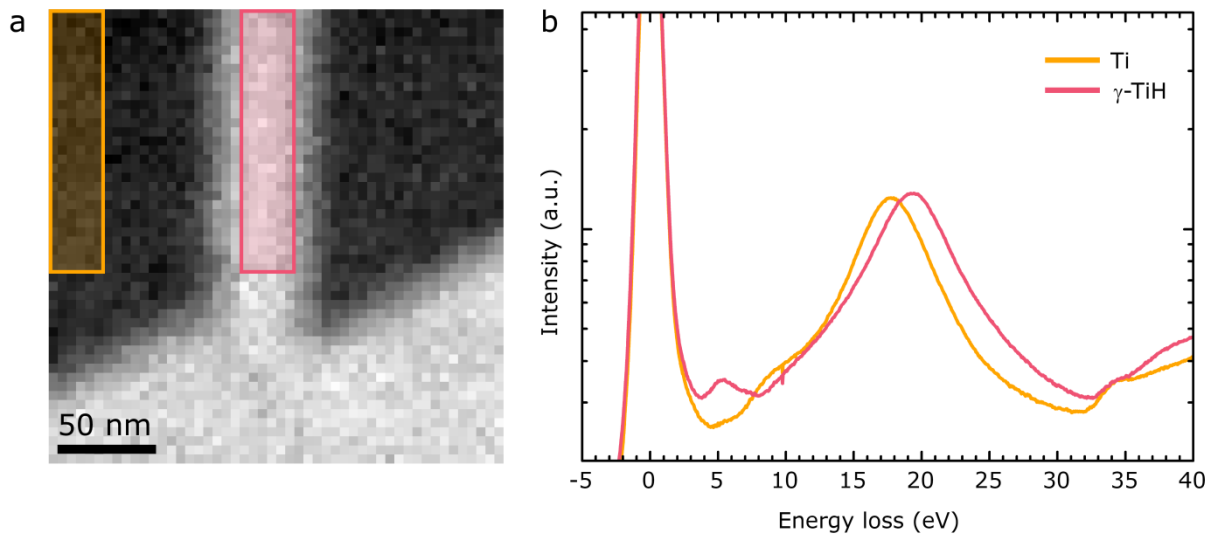

Figure S5: *(a) Intensity map (with an energy window from 19.80 eV to 19.85 eV) shows the area from which we extracted the electron energy loss spectra. The γ-TiH precipitates appear with higher intensity compared to the darker Ti matrix due to the filtering. (b) The equally sized yellow and pink areas in (a) are integrated to yield the spectra for respectively α-Ti and γ-TiH. The peaks close to 20 eV correspond the plasmon peaks, and are a fingerprint for the two phases.*

From the high electron energy loss part of the spectrum we investigated if contaminants/dopants are present because titanium has a high affinity for carbon, nitrogen and oxygen (**Figure S6**). The spectrum only contains an ionization edge starting at 456 eV which belongs to Ti $L_{2,3}$ edge (462 eV and 456 eV, respectively), and no signs of carbon, nitrogen and/or oxygen are present in the spectrum, because the C K edge (284 eV), N K edge (401 eV) and O K edge (532 eV) are

missing. Hence, based on the EELS analysis we conclude that titanium hydride precipitates are present without any noticeable contaminants/ dopants.
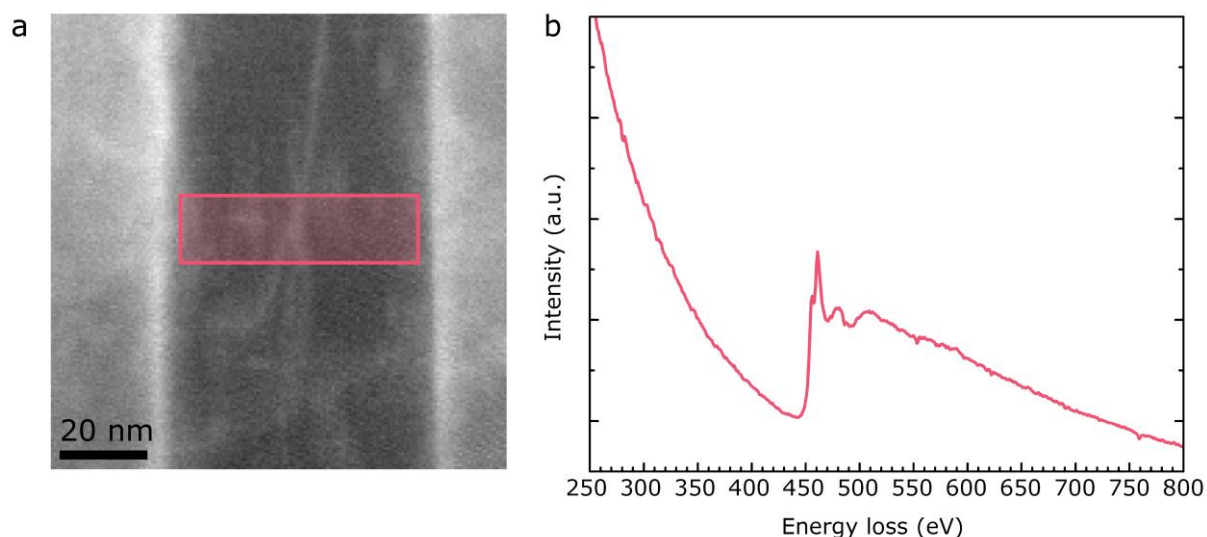

Figure S6: (a) Overview image of the area from which we acquired an electron energy loss spectrum. The actually scanned area of the spatially resolved spectrum was the same height as the pink highlighted area, but slightly wider to extend into the Ti matrix. (b) Integrated high-loss spectrum from the pink area in the γ-TiH precipitate as depicted in (a) is plotted. The absorption edges of C, N, O and Ti are located in this energy range but not detected as only the sharp edge from Ti is visible.

3. Scanning transmission electron microscopy

For the atomic resolution imaging we used a probe and image corrected Themis Z S/TEM operating at 300 kV. Images were recored with convergence semi-angle of 21 mrad and a probe current of 50 pA (Figure 2 of the main article) and 14 pA (Figure 5 of the main article), a step size between 5 and 20 pm, image resolution of 1024x1024 pixels up to 4096x4096 pixels and a pixel dwell time of 1 up to 10 μs. The acquired iDPC images in Figure 2c and Figure 5b of the main article are filtered with a high-pass Gaussian filter with a standard deviation of 1.1 nm^{-1} that corresponds to 10% of the bright-field disk size of 21 mrad. The HAADF and ABF images in Figure 2a-b and Figure 5a,c of the main article are filtered using an average background subtraction filter [5] (freely available at http://www.dmscripting.com/hrtem_filter.html).

4. Multislice scanning transmission electron microscopy simulations

The three-dimensional models of γ-TiH and its interface with α-Ti are constructed with VESTA [7]. The lattice parameters of freestanding γ-TiH are set to a=4.20 Å and c=4.60 Å and those of α-Ti to a=2.9508 Å and c=4.6855 Å [2]. For the models of the interface the γ-TiH unit cell is slighty adjusted by -0.6% for the a lattice parameter (a=4.1730 Å) and +1.9% for the c lattice parameter (c=4.6855 Å) to obtain a perfect coherent interface with the α-Ti where the interface plane is formed by $(01-10)_\alpha//(1-10)_\gamma$ and where in-plane the $[0001]_\alpha//[001]_\gamma$ (and $[-2110]_\alpha//[110]_\gamma$) directions are parallel.

These models are loaded in software for multislice simulations called Dr. Probe [8]. The models are always one unit cell thick and are cut in four equally thick slices. With this approach each slice contains one atomic plane in the case of γ-TiH (alternating Ti and H planes), whereas the α-Ti phase contains two emtpy slices and two Ti planes (alternating Ti and empty planes) as no atoms are present at z=1/4 and z=3/4. Atomic vibrations are accounted for with the frozen-lattice method, where the used Debye-Waller factors at 300 K are 0.52 $Å^2$ for Ti and 5.0 $Å^2$ for H. The factor for Ti is taken from the table in the work of Peng et al. [9], while we linearly extrapolated the Debye-Waller factor for H from the same table using the listed group I elements. It is assumed that the microscope has no aberrations except for defocus, and the operating conditions are set equal to the experimental settings of 300 kV and a convergence angle of 21 mrad. In experiment, the corrector software reduces the high order abberations to values close to zero, the first order aberrations (A1 and C1) to values below 0.5 nm and second order aberrations (A2 and B2) to values in the range of 5 nm. The probe step size is set to 10 pm or lower, depending on the size of the simulated image. The used detectors are given in the table below, which are equivalent to the calibrated experimental values. The final simulated ABF and HAADF images are then convolved with a two dimensional Gaussian function of 70 pm FWHM to account for the finite probe size. In addition to the normal ABF image, we also add the images from the four quadrant detectors to obtain an ABF-like image that we call DPC sum. The difference is that the inner collection angle is a bit smaller, and the outer collection angle extends into the dark field part of the diffraction pattern.

Detector name	Azimuthal range (°)	Inner collection angle (mrad)	Outer collection angle (mrad)
DPC_A	-45 − 45	10	40
DPC_B	45 − 135	10	40
DPC_C	135 − 225	10	40
DPC_D	225 − 315	10	40
ABF	0 − 360	11	18
HAADF	0 − 360	43	200

The images from the DPC_(A-D) detectors, however, are first processed to obtain the iDPC image, according to the method described in the work of Lazic et al. [10]. This processing procedure is as follows: first the opposite segments are subtracted (i.e. DPC_A − DPC_C and DPC_B − DPC_D, in the detector coordinates system) to obtain the orthogonal (x,y) differential phase contrast (DPC) images DPC_x and DPC_y by rotating the vector components to match the scanning (image) coordinates system[11]. Periodic boundary conditions are constructed for the (non-periodic) interface by mirroring the DPC_x and DPC_y images, which is necessary to prevent aliasing effects for the simulations that cover a small field-of-view[12]. Next, the DPC_x and DPC_y images are integrated in the Fourier domain to obtain the Fourier transformed iDPC image:

$$\mathcal{F}\{iDPC(x,y)\}(k_x,k_y) = \frac{k_x \cdot \mathcal{F}\{DPC_x(x,y)\}(k_x,k_y) + k_y \cdot \mathcal{F}\{DPC_y(x,y)\}(k_x,k_y)}{2\pi i(k_x^2 + k_y^2)}$$

Where k_x and k_y are the orthogonal k-vector components in the Fourier domain. The intensity in the Fourier transformed iDPC image at $k_x = k_y = 0$ is set to 0 to account for the singularity, before inverse Fourier transforming to obtain the real space iDPC image. Note that this is merely a constant that shifts the intensity of the image. Next, the iDPC image is convolved with the two dimensional Gaussion function of 70 pm FWHM to account for the finite probe size.

The iDPC image, that is corrected for the finite probe size, is used to obtain the DPC vector image and dDPC scalar image. The DPC image is obtained from the gradient of the iDPC image, which returns the two in-plane (x,y) vector components of the DPC image. This provides a physically regularized DPC image, where the non-conservative part of the noise is removed[10,11].

Differentiating once more, by applying the diverence operator to the DPC vector image, yields the dDPC scalar image.

5. Multislice simulations of the γ-TiH unit cell with and without hydrogen atoms

In this section we show that the observed peaks in the experimental images, as depicted in Figure 4 of the main article, are indeed a result of the hydrogen atoms, instead of being an image artifact that stems from interference effects. For this purpose, we have simulated the γ-TiH unit cell with hydrogen atoms and without hydrogen atoms. In **Figure S7** we present the simulated ABF, DPC sum and iDPC images for the empty (Figure S7a) and filled (Figure S7b) γ-TiH unit cell. In this figure the intensity profile along the face diagonal (Figure S7a), or a combined result of the two face diagonals (Figure S7b) is mapped as a function of thickness. In this way the intensity profile contains three Ti atomic columns and two empty columns in Figure S7a, and three Ti atomic columns, one empty column and one hydrogen atomic column in Figure S7b. The lower half of the figure shows the simulated images for a selection of specimen thickness' in steps of 9.2 nm (or 20 unit cells).
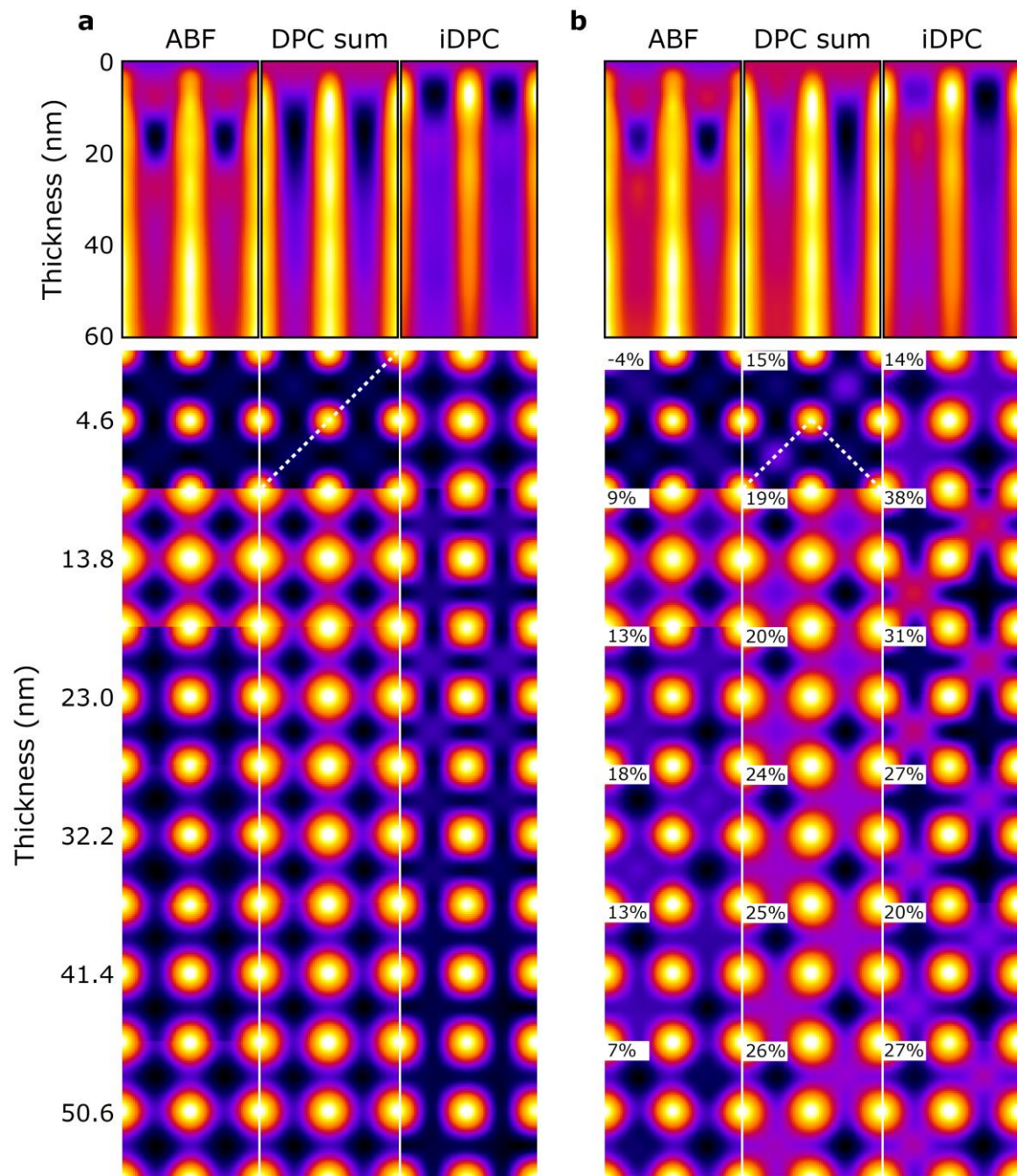
Figure S7: *Simulated ABF (Δf=0 nm), DPC sum (Δf=0 nm) and iDPC (Δf=-4 nm) images of the γ-TiH unit cell images are compared. At the top part the intensity profiles (along the indicated white dashed line indicated below) as a function of thickness are shown. The bottom part shows the γ-TiH unit cell **(a)** without hydrogen atoms, and **(b)** with hydrogen atoms for various thicknesses. In (b) the relative hydrogen intensity is inset. The contrasts of the ABF and DPC sum images are inverted to ease the visual comparison.*

In case of the ABF and DPC sum images, four broad peaks are present between the Ti columns in Figure S7a for crystals thinner than about 12 nm and 6 nm, respectively. The iDPC image also shows this feature but for crystals with a thickness around 15-25 nm. This demonstrates that when no hydrogen atoms are present, the erroneous conclusions can be drawn that a dihydride crystal has been imaged, where the four tetrahedral columns are filled with hydrogen atoms.

The simulated images of the normal γ-TiH unit cell (Figure S7b) shows that the hydrogen columns can be imaged by the three methods since relatively bright peaks at the expected position are observed in all cases. The highest relative intensity of the hydrogen columns is achieved with iDPC, followed by DPC sum and least with ABF. In the case of ABF the crystal should be thinner than about 35 nm, otherwise the intensity from the hydrogen column is drastically reduced. The DPC sum image is able to transfer the signal from the hydrogen column with a rather stable contrast even for relatively thick specimen. However, the intensity at the location of the hydrogen column does not resemble a well defined peak. This is clearly better in case of iDPC, where the contrast of the hydrogen column is the highest, and also a well defined peak shape occurs.

Results like shown Figure S7b hold for single defocus values. We repeated this for different defocus values and quantitatively analyzed and plotted all results in **Figure S8**, **Figure S9** and **Figure S10**, for ABF, DPC sum and iDPC imaging, respectively. In Figure S8a,b the relative intensity of the hydrogen column and titanium column w.r.t. the empty column is plotted. This indeed shows that for ABF imaging the contrast reversal of the hydrogen and empty column at zero defocus (which is the operating value in experiment) for crystals thinner than about 10 nm. For more negative defocus, the contrast reversal increases in magnitude and extends to slightly thicker crystals, and also the contrast between the titanium column and empty column is reversed. For more positive defocus the contrast between the titanium column and empty column is again reversed. Hence, for ABF imaging it is crucial to stay close ($\Delta f=\pm 4$ nm or smaller) to zero defocus.

The same result is shown in Figure S9, but now for the DPC sum image. This result is similar to the case of ABF, but with slightly less oscillatory behaviour. The contrast reverses between the hydrogen and empty column only for negative defocus values for crystals thinner than about 10-20 nm. However, the contrast reverses between the titanium column and the empty column for

both positive and negative defocus values. In Figure S9c it is also appearant that the relative intensity of the hydrogen column w.r.t. the Ti column is remarkably independent from the crystal thickness, as has been shown in Figure S7b. However, also for DPC sum imaging it is crucial to stay close ($\Delta f=\pm 4$ nm or smaller) to zero defocus.

Finally, the analysis of the iDPC imaging is shown in Figure S10. Contrast reversals between the titanium and empty column occur for all positive defocus values, and occur between the hydrogen and empty column for positive defocus values larger than 4 nm. However, for negative defocus values there are no contrast reversals, except for crystals thinner than about 4 nm for the most negative defocus value of -8 nm that we simulated. Physically this means that in the case of iDPC it is important to focus the probe into the specimen i.e. below the top surface. The value of the defocus is only limited by the specimen thickness, as it is the depth at which the projected electrostatic potential is probed by the converged beam waist allowing atomically resolved 3D iDPC imaging [13]. In addition, it shows enhanced contrast between the hydrogen and titanium columns as plotted in Figure S10c.

The above image simulations clearly demonstrate that iDPC imaging provides better results than ABF and DPC sum imaging with best localization and highest contrast of the hydrogen column, largest thickness and defocus ranges without disturbing contrast reversals and oscillatory behavior.
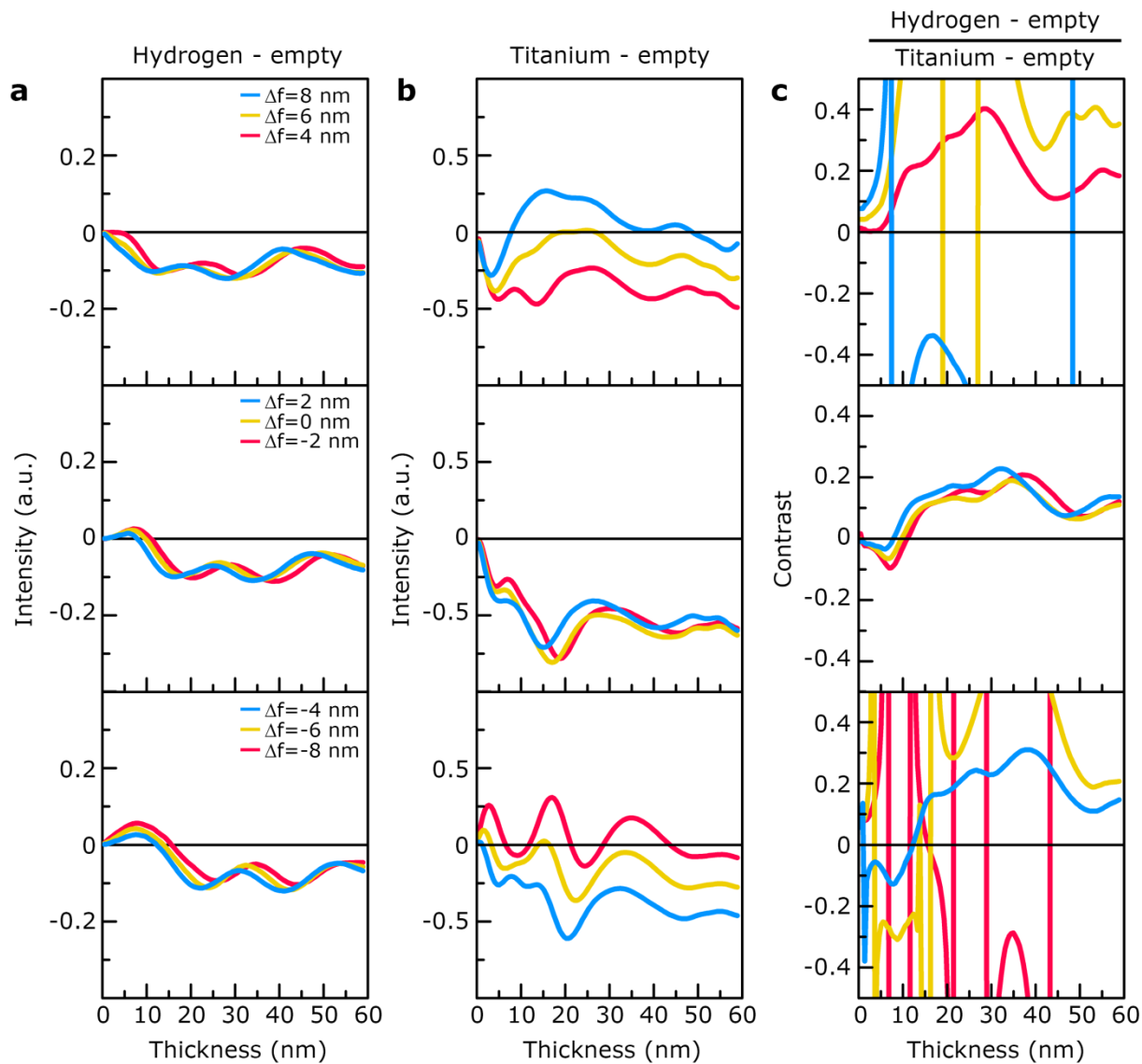
Figure S8*: Simulated ABF images of the γ-TiH unit cell are quantitatively analysed. The relative intensities of the (**a**) hydrogen and (**b**) titanium column w.r.t. the empty column are plotted as a function of crystal thickness for various defocus settings. The ratio of the former two defines the relative intensity of the hydrogen column in (**c**). We classified the results in three defocus windows: negative (-8 nm to -4 nm), close to zero (-2 nm to +2 nm), positive (+4 nm to +8 nm). The vertical scale limits are (a) -0.4 to 0.4 (b) -1.0 to 1.0 (c) -0.5 to 0.5 and allow direct comparison of Figures. S8, S9 and S10.*
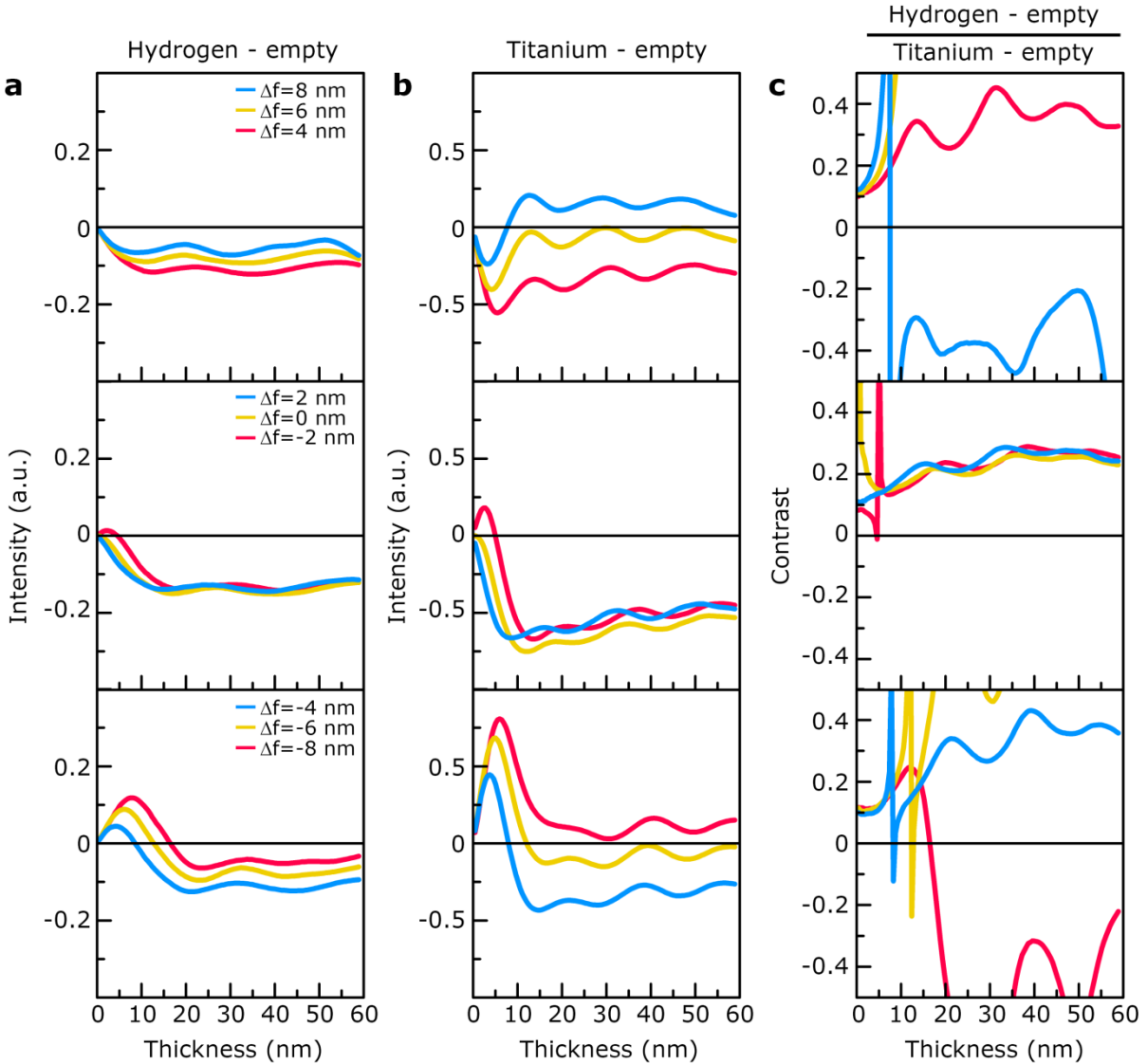
Figure S9*: Simulated DPC sum (ABF-like) images of the γ-TiH unit cell are quantitatively analysed. The relative intensities of the (**a**) hydrogen and (**b**) titanium column w.r.t. the empty column are plotted as a function of crystal thickness for various defocus settings. The ratio of the former two defines the relative intensity of the hydrogen column in (**c**). We classified the results in three defocus windows: negative (-8 nm to -4 nm), close to zero (-2 nm to +2 nm), positive (+4 nm to +8 nm). The vertical scale limits are (a) -0.4 to 0.4 (b) -1.0 to 1.0 (c) -0.5 to 0.5 and allow direct comparison of Figures. S8, S9 and S10.*
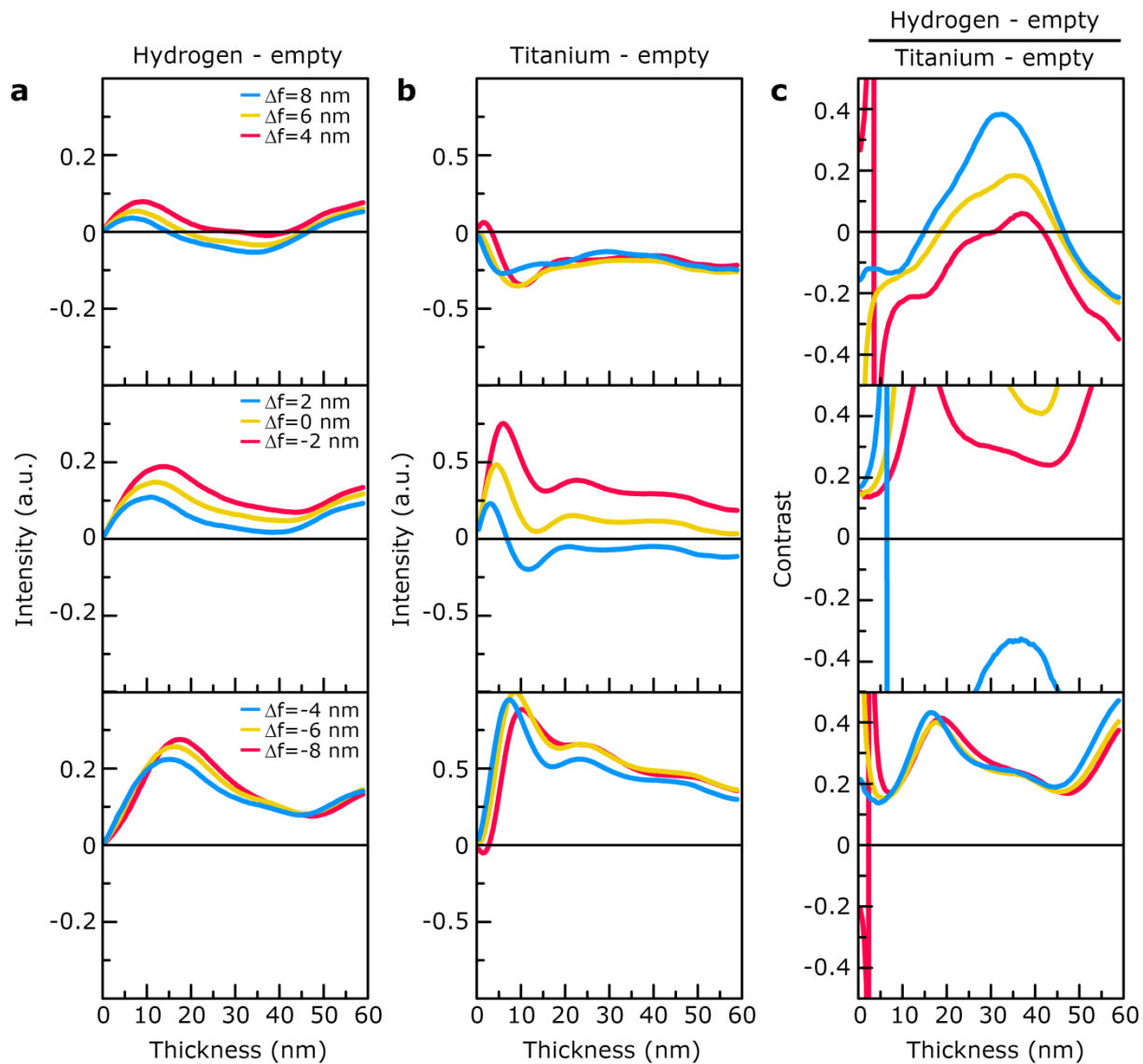
Figure S10*: Simulated iDPC images of the γ-TiH unit cell are quantitatively analysed. The relative intensities of the **(a)** hydrogen and **(b)** titanium column w.r.t. the empty column are plotted as a function of crystal thickness for various defocus settings. The ratio of the former two defines the relative intensity of the hydrogen column in **(c)**. We classified the results in three defocus windows: negative (-8 nm to -4 nm), close to zero (-2 nm to +2 nm), positive (+4 nm to +8 nm). The vertical scale limits are (a) -0.4 to 0.4 (b) -1.0 to 1.0 (c) -0.5 to 0.5 and allow direct comparison of Figures. S8, S9 and S10.*

6. Multislice simulations of the tilted γ-TiH unit cell with and without hydrogen atoms

In the experiments the local alignment of the specimen was constrained by the small length scale crystal bending. From the experimental images usually only a small part was well aligned, which we assessed based on the combined quality of the HAADF and iDPC or ABF images. The combined effect of crystal tilt and the wave character behaviour of particularly the iDPC and ABF imaging could potentially induce imaging artefacts that lead to erroneous detection of atomic columns. Therefore, we investigate if crystal tilt can introduce peaks in the image that could be wrongly attribed to hydrogen atomic columns.

To this purpose we have performed multislice image simulations of a titled γ-TiH unit cell, with and without the hydrogen atoms. We applied a crystal tilt of 0.5° (8.7 mrad) in x and y direction (i.e. the unit cell is tilted along a face diagonal), as these were approximately the maximum misalignments we encountered in experiments, especially near the interface. The reason why we chose to tilt the crystal along the face diagonal is that crystal tilt in the x or y direction would certainly not generate the asymmetry of intensity peaks that we observe (i.e. this wil not produce the ordered {110} type of intensity peaks).

We present the results of these image simulations in **Figure S11** in the same way as we presented Figure S7. However, now we show the intensity profile of the entire face diagonal only in the tilt direction in Figure S11b, instead of the combined profile of both diagonals like we presented in Figure S7b. We cannot use the intensity profile of the other (anti-)diagonal due to streaking of the titanium atomic columns. The intensity maps at the top panel can be used to compare the empty (Figure S11a) and hydrogen (Figure S11b) columns.

For the three imaging techniques the titanium atomic columns in Figure S11a have asymmetric shapes as a consequence of the crystal tilt. The titanium atomic columns also appear to be displaced with respect to to their actual position. This effect is mostly visible for ABF and DPC sum, and only minimally for iDPC where the atomic columns remain most localized. Furthermore, the apparent position of the atomic columns are very sensitive to thickness and can show relatively large jumps for minor increases in crystal thickness. This is most visible for DPC sum and ABF for about 15 nm thick crystal, and again at around 40 nm.

More relevent is that the empty unit cell (see Figure 11a) contains apparent atomic columns between the titanium columns only for the DPC sum image, and not for ABF and iDPC images. When the crystal is not tilted, there are apparent atomic columns for all three imaging techniques. Hence, when the crystal is tilted, interference effects are reduced for ABF and iDPC, but not for DPC sum. When hydrogen atoms are present (see Figure S11b) then only DPC sum and iDPC show visible contrast between the hydrogen and empty column, and ABF does not. The resulting checkerboard-like pattern remains most clearly visible when the crystal is thinner than about 30 nm for DPC sum imaging, as the contrast reduces for thicker crystals. Whereas the contrast remains best for iDPC imaging even for thick crystals.

Overall, these result demonstrates that iDPC imaging is least sensitive towards crystal tilt on several aspects. iDPC imaging shows the least atomic column displacement, and remains capable of imaging hydrogen atomic columns even for thick crystals despite the rather extreme crystal tilt. In contrast, ABF and DPC sum imaging show substantial displacement and also sudden jumps in apparent atomic column position. Furthermore, ABF imaging is not able to transfer any significant signal from the hydrogen columns and DPC sum imaging can do this only for crystals thinner than about 30 nm.
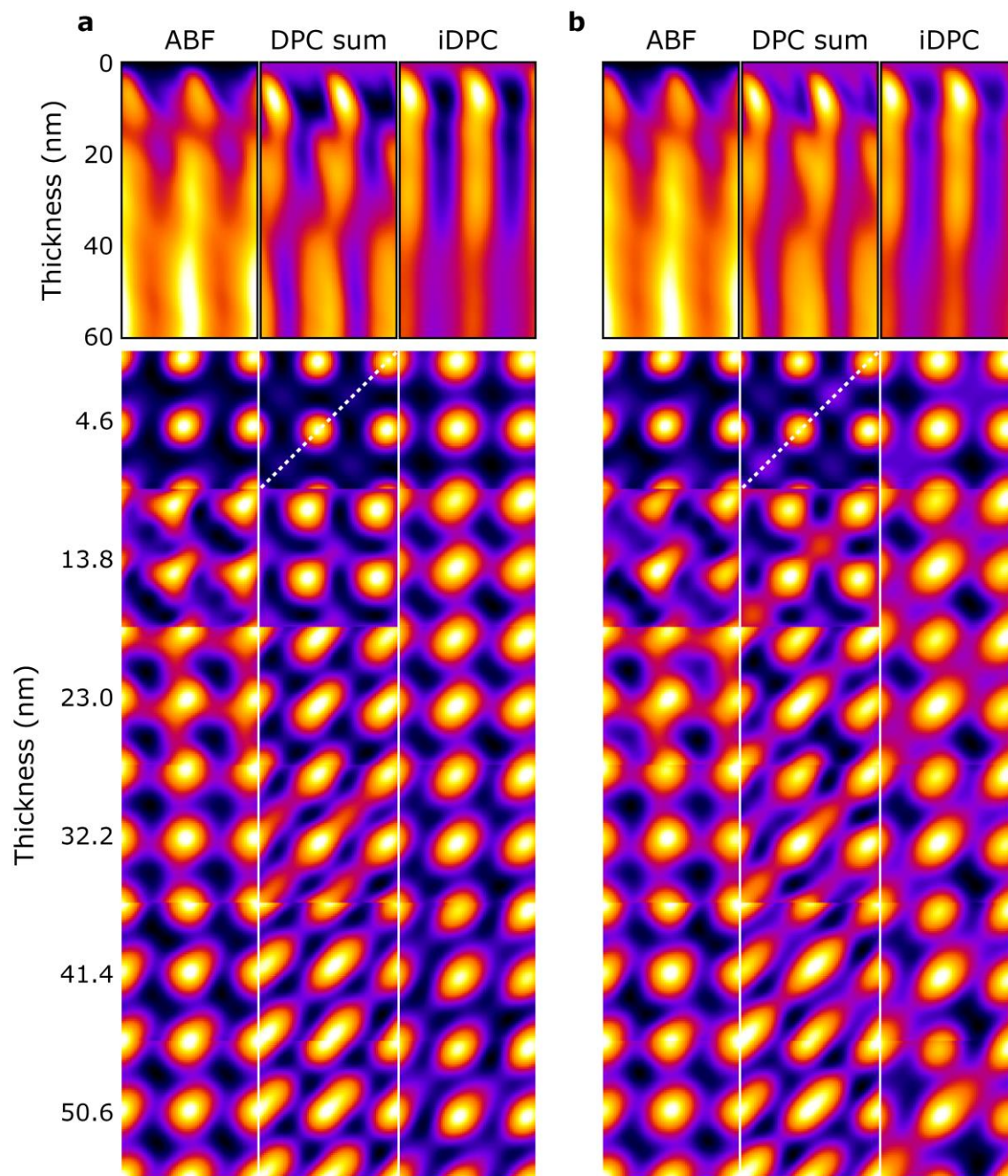
Figure S11: Simulated ABF (Δf=0 nm), DPC sum (Δf=0 nm) and iDPC (Δf=-4 nm) images of the tilted γ-TiH unit cell images are compared. On the top the intensity profiles (along the indicated dashed line below) as a function of thickness are shown. The bottom shows the γ-TiH unit cell **(a)** without hydrogen atoms and **(b)** with hydrogen atoms. The contrast of the ABF and DPC sum images are inverted to ease the visual comparison.
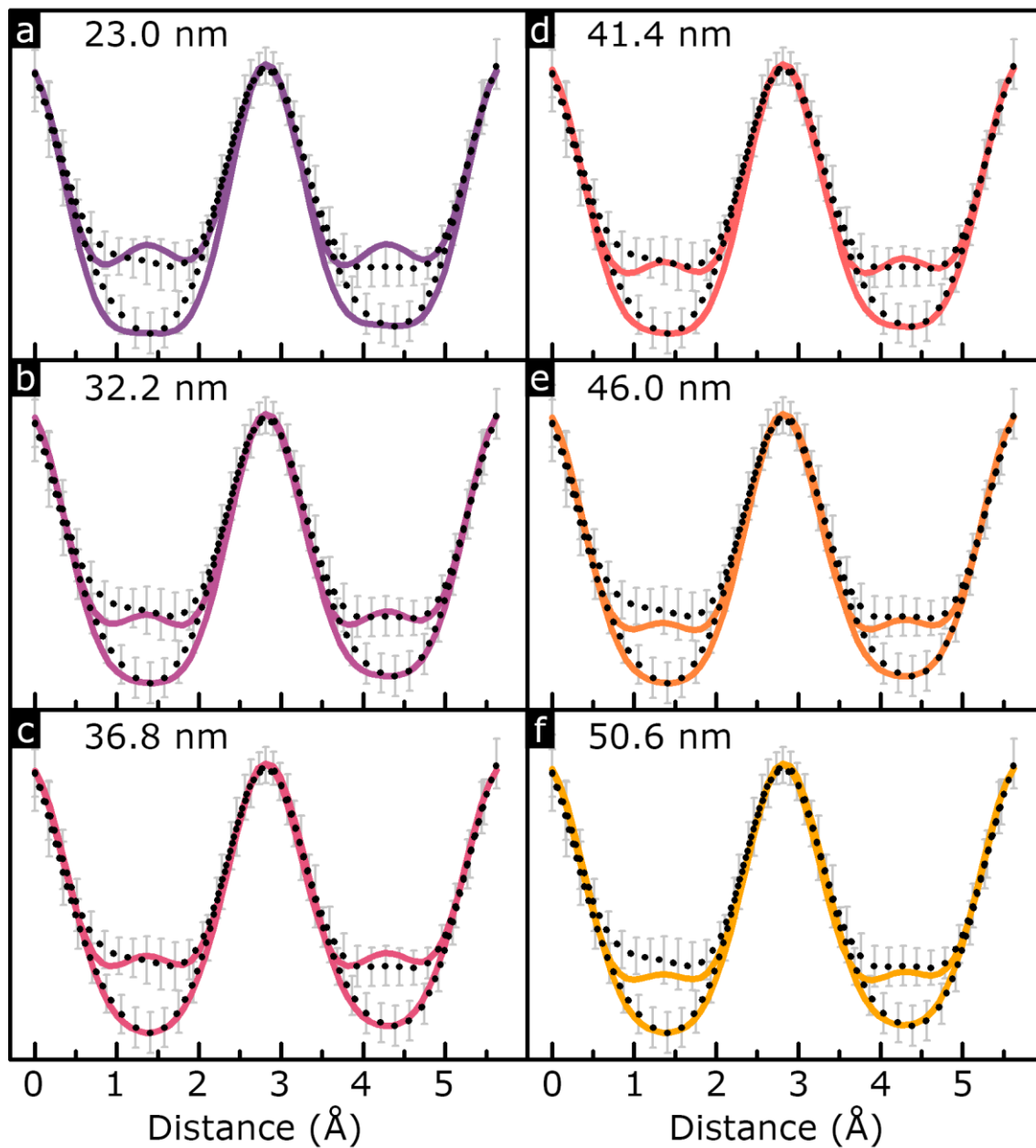
Figure S12: Normalized intensity profiles from the simulated (solid coloured lines) iDPC image (Δf=-4 nm) are compared with the line profiles from the experimental (dotted black lines) image of Fig. 2c from the main article. The simulated specimen thicknesses are **(a)** 23.0 nm, **(b)** 32.2 nm **(c)** 36.8 nm **(d)** 41.4 nm **(e)** 46.0 nm and **(f)** 50.6 nm. Vertical scale ranges from -0.1 to 1.15.

References

1. Bourret, A., Lasalmonie, A. & Naka, S. In-situ high resolution observation of hydride precipitation in titanium. *Scr. Metall.* **20**, 861–866 (1986).

2. Numakura, H. & Koiwa, M. Hydride precipitation in titanium. *Acta Metall.* **32**, 1799–1807 (1984).

3. Yan, L., Ramamurthy, S., Noël, J. J. & Shoesmith, D. W. Hydrogen absorption into alpha titanium in acidic solutions. *Electrochimica Acta* **52**, 1169–1181 (2006).

4. Ding, R. & Jones, I. P. In situ hydride formation in titanium during focused ion milling. *J. Electron Microsc. (Tokyo)* **60**, 1–9 (2011).

5. Kihn, Y., Mirguet, C. & Calmels, L. EELS studies of Ti-bearing materials and ab initio calculations. *J. Electron Spectrosc. Relat. Phenom.* **143**, 117–127 (2005).

6. Kilaas, R. Optimal and near-optimal filters in high-resolution electron microscopy. *J. Microsc.* **190**, 45–51 (1998).

7. Momma, K. & Izumi, F. VESTA 3 for three-dimensional visualization of crystal, volumetric and morphology data. *J. Appl. Crystallogr.* **44**, 1272–1276 (2011).

8. Barthel, J. Dr. Probe: A software for high-resolution STEM image simulation. *Ultramicroscopy* **193**, 1–11 (2018).

9. Peng, L.-M., Ren, G., Dudarev, S. L. & Whelan, M. J. Debye–Waller Factors and Absorptive Scattering Factors of Elemental Crystals. *Acta Crystallogr. A* **52**, 456–470 (1996).

10. Lazić, I., Bosch, E. G. T. & Lazar, S. Phase contrast STEM for thin samples: Integrated differential phase contrast. *Ultramicroscopy* **160**, 265–280 (2016).

11. Lazić, I. & Bosch, E. G. T. Chapter Three - Analytical Review of Direct Stem Imaging Techniques for Thin Samples. in *Advances in Imaging and Electron Physics* (ed. Hawkes, P. W.) **199**, 75–184 (Elsevier, 2017).

12. Ishizuka, A., Oka, M., Seki, T., Shibata, N. & Ishizuka, K. Boundary-artifact-free determination of potential distribution from differential phase contrast signals. *Microscopy* **66**, 397–405 (2017).

13. Lazić, I., Bosch, E. G. T., Yucelen, E., Imlau, R. & Sorin, L. Thick (3D) Sample Imaging Using iDPC-STEM at Atomic Scale. *Microsc. Microanal.* **24**, 170–171 (2018).